Supercapacitor Characterization Using Universal Adaptive Stabilization and Optimization

SHAYOK MUKHOPADHYAY [iD] [1] **(Member, IEEE), RACHED DHAOUADI**[1] **(Senior Member, IEEE),**
MOHANNAD TAKROURI[2] **(Member, IEEE), AND RAVEENDHRA DOGGA**[1] **(Member, IEEE)**

[1] Department of Electrical Engineering, American University of Sharjah, Sharjah 26666, UAE
[2] Alumnus of the Mechatronics Engineering Graduate Program, American University of Sharjah, Sharjah 26666, UAE

CORRESPONDING AUTHOR: SHAYOK MUKHOPADHYAY (e-mail: smukhopadhyay@aus.edu).

ABSTRACT This paper presents a simplified supercapacitor model and a universal adaptive stabilization, optimization (UAS+O) based parameter identification technique. Analytic solutions for the description of supercapacitors current, voltage, subject to cyclic voltage and current sources of varying amplitudes and frequency, consistent with electric vehicle driving cycles, are developed. Supercapacitor I-V relationships show hysteresis, indicating simultaneous energy storage and dissipation mechanisms. A reduced equivalent circuit model is proposed to accurately represent hysteresis I-V characteristics. The proposed UAS+O based technique for estimating model parameters, is supported by mathematical proofs, simulation, and experimental results.

INDEX TERMS Hysteresis loop, optimization, parameter identification, supercapacitor, universal adaptive stabilization.

I. INTRODUCTION

Supercapacitors have received a lot of attention recently and are being considered as a viable auxiliary power source due to their outstanding power characteristics. They have been integrated successfully with energy storage systems for many industrial applications such as electric vehicles and photovoltaic energy systems. The inclusion of supercapacitors (SCs) can be very useful to maintain stability in electrical power systems by enhancing the energy supply from batteries and intermittent renewable resources [1]–[4].

To facilitate the integration of supercapacitors with batteries and electric vehicles, an accurate dynamic model is needed to represent the static and dynamic behavior of SCs. Such equivalent models will be useful to determine the state of charge and power capability of the energy storage system and enable efficient energy management, and scheduling of future electric vehicle power sources. It is also desirable to have an equivalent model which is not complex to allow a practical parameter identification and a relatively simple commissioning procedure of a supercapacitor enabled electric vehicle system.

Many methods have been used in the literature to derive an equivalent model of SCs. These methods may be classified according to several categories, such as time-domain identification of interleaved RC circuit models [5]–[9]; frequency-domain identification by impedance spectroscopy models [10]–[15]; or electrochemical thermal principle identification models [16], [17]. In much of the literature, the equivalent model is based on the analysis of the physical and electrochemical structure of carbon-based supercapacitors. It is well understood as a first approximation that the higher capacitance value is mainly due to the very large effective surface area of the porous activated carbon electrodes. On the other hand, the charge buildup in the different regions on the electrode area is not homogenous under a rapid charging or discharging phase. The charge takes significantly different amounts of time to migrate to, or from the different regions of the electrode areas through the porous surfaces. As a result, charge redistribution side effects are encountered such as open circuit voltage decay, capacitance loss at high frequency, and voltammetric distortions at high scan rates [7], [8].

The accurate modelling of SCs is a challenging problem and several techniques exist for supercapacitor modeling and parameter identification depending on the application [18]–[21]. The authors use work related to UAS based voltage collapse detection, and parameter identification of Li-ion batteries [22]–[24] as a motivation to propose UAS based supercapacitor parameter identification in this work. Complex and accurate models exist for batteries, for which parameter identification requires a lot of experimental effort. So, the work in [23], [24] successfully identifies parameters of a reasonably accurate model with reduced experimental effort, and without extensive computational effort, via UAS. Similarly, there are several nonlinear models that have been formulated for supercapacitors, including fractional order models and associated parameter identification techniques, which were shown to be accurate. However often, the parameter identification for such models needs several linearization steps and needs substantial experimental effort. Therefore, this work proposes a reduced order supercapacitor model, which is reasonably accurate when combined with the proposed UAS+O strategy. Additionally, the proposed approach enables estimation of supercapacitor model parameters within a single experimental run, and without extremely expensive computational requirements.

Electro-analytical methods are a class of techniques in analytical chemistry which study and analyze electrochemical cells, such as batteries and capacitors, by measuring the potential (volts) and/or current (amperes) in the cells [17]. These methods can be broken down into several categories depending on which aspects of the cell are controlled and which are measured. The three main categories are potentiometry (the difference in electrode potentials is measured), coulometry (the cell's current is measured over time), and voltammetry (the cell's current is measured while actively altering the cell's potential).

A universal equivalent circuit model was presented for carbon-based supercapacitor cells [7]. This circuit explains the three most significant performance-limiting features of present-day devices, namely open circuit voltage decay, capacitance loss at high frequency, and voltammetric distortions at high scan rate. In addition, the circuit reproduces the complex plane impedance behavior of supercapacitors and also reveals why the equivalent series capacitance increases with temperature.

This work develops analytic expressions for cyclic voltammetry and triangular current sweep chrono-potentiometry of supercapacitors that can be represented by a reduced order equivalent circuit model. Further this work proposes a novel supercapacitor parameters estimation methodology based on universal adaptive stabilization (UAS) and optimization. UAS, and the simplified model structure, is chosen because it has been successfully used for parameter identification and fault detection in energy storage devices [22]–[24]. The works in [22], [23] use a version of UAS which require manual guessing of initial values of model parameters, this process can be time consuming. This is fixed in this paper by combining the UAS based strategy with an optimization procedure which runs iteratively. The main motivation behind this work is to avoid having to treat each supercapacitor branch separately, and then identify distinct events by looking at the V-I characteristics, a process common in the literature [5]. Although the above process produces results [5], identifying the discrete 'events' requires experience, and also requires making many assumptions. The main advantage of the UAS+O based technique is that no such 'events' need to be identified. This can lead to increased model parameter identification accuracy, because identification of such 'events' can be subjective, and therefore prone to operator error.

There exist fractional order models for supercapacitors [11], while they may be accurate, such models can be complex for execution on limited computational capability available on small mobile robots or drones. An RC ladder-network provides a standard model for the internal porous structure of a supercapacitor [7], and also can be used to model and implement fractional order transfer functions [25]–[27]. Fractional order models of supercapacitors in the literature [28], also frequently incorporate RC ladder networks. Further, for practical usage, the value of a supercapacitors's equivalent capacitance can be considered to be slowly varying. The above insights are used in this paper to propose a simplified equivalent circuit of a supercapacitor, whose parameters are treated as constants in the short-term, and therefore can be easily identified automatically via a UAS based algorithm. This is further augmented with an optimization procedure, which estimates an equivalent RC ladder network model for a supercapacitor. The proposed model is simple enough to enable online model parameter identification, and implementation on a low cost computing system found on mobile robots, or drones. So, even though the paper uses a constant parameter based model, the adaptive procedure followed by the optimization process can be used to regularly update the model parameters as needed, so that any change in a supercapacitor's model parameters during real-life operation can be easily accounted for, and the RC ladder structure chosen provides benefits associated with fractional order supercapacitor models, as mentioned in Section VI.
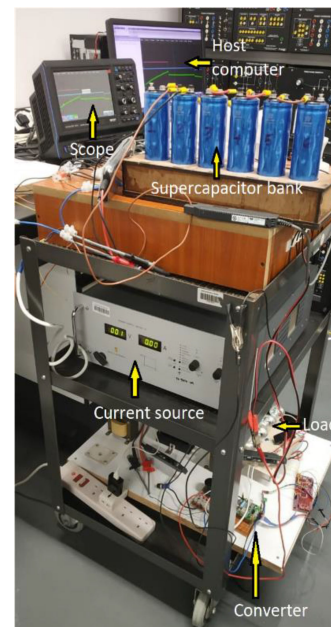
The remainder of this paper is organized as follows. Section II presents the results of initial cyclic voltammetry tests which show sample I-V characteristics experimentally obtained using our supercapacitors. These I-V characteristics are used to validate the parameter estimation methodologies proposed in this paper. Section III presents a method to identify parameters of a supercapacitor model based on analytical expressions of supercapacitor step and ramp response. Section IV presents the UAS+O based parameter estimation methodology. Sections V, and VI present the experimental results related to supercapacitor parameter identification via the methods proposed in this paper. Section VII presents comparison with an existing approach. Section VIII, and IX discuss advantages and provide concluding remarks. Proofs of mathematical results are in the appendix.

(a)

(b)
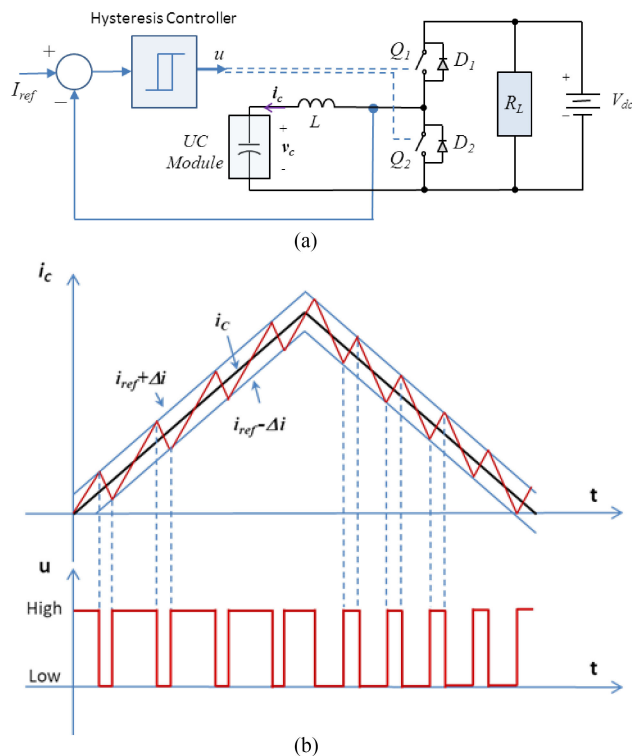
FIGURE 1. (a) Block diagram of the proposed SC test bench. (b) Principle of operation of hysteresis current control.

FIGURE 2. Hardware setup of the SC test bench.

II. EXPERIMENTAL SETUP AND CYCLIC VOLTAMMETRY TESTS

Fig. 1(a) shows the proposed experimental setup used to perform cyclic voltammetry and triangular current sweep chronopotentiometry on the supercapacitors (SCs). The system uses a battery as the main DC power source. The SC module is interfaced to the DC bus through a bidirectional DC/DC converter to control the energy transfer between the battery and the SC module. A variable resistance is used as the main load. The circuit is controlled through a PWM signal generated by a hysteresis current controller. The two switches Q1 and Q2 are power MOSFET devices that are switched in a complementary mode (Q1 on and Q2 off or Q1 off and Q2 on). Both switches cannot be turned on simultaneously, this is done to avoid a short circuit of the battery. The diodes D1 and D2 act as freewheeling diodes to allow continuous conduction of the inductor current during switching. The design of a hysteresis current controller consists of selecting the hysteresis band Δi that defines the range of the inductor current variation around the reference value. Every time the error between the reference current and actual current crosses either the positive or negative hysteresis band's boundary, a change in the PWM signal occurs to change the converter voltage and force the current reversal as shown in Fig. 1(b). Thus, the controller quickly reacts to any deviation from the reference signal, which is the reason why the hysteresis controller is referred to as a high gain controller. Referring to Fig. 1, let $e = I_{ref} - i_c$. If $i_c \geq I_{ref} + \Delta i \rightarrow e \leq -\Delta i$ Then, the PWM signal $u =$

$Low \rightarrow Q_1 \ off$ and $Q_2 \ on$. If $i_c \leq I_{ref} - \Delta i \rightarrow e \geq \Delta i$. Then, the PWM signal $u = High \rightarrow Q_1 \ on$ and $Q_2 \ off$. Hysteresis current control is widely used due to its simplicity in implementation as well as its fast and accurate response. However, the main issue is its variable switching frequency which leads to extra switching losses and the injection of high-frequency harmonics into the system. The current can be also controlled using PID control with a fixed PWM modulator, which will have the advantage of constant switching frequency. However, hysteresis current control has more desirable characteristics such as high stability and fast and accurate dynamic behaviour. The power converter regulates the energy flow to and from the SC in two modes of operation: buck mode and boost mode, depending on the direction of the inductor current. The actual hardware setup is shown in Fig. 2. The bidirectional DC-DC converter is implemented using the Open Source Motor Control (OSMC) board, which is an H-Bridge with a maximum rating of 36 V, 160 A and 20 kHz [36]. To determine the I-V characteristics of the SC, two tests are performed: chrono-potentiometry test and cyclic voltammetry test. In the chrono-potentiometry test, the current is controlled to vary in a triangular manner with a given frequency and amplitude, and the resulting voltage is measured and recorded. Fig. 4, shows the I-V characteristics for a constant current amplitude and three different sweep rates. The current and voltage vs. time for one of the curves in Fig. 3 is shown in Fig. 5. Also, an example of a chrono-potentiometry test with a 4 A current amplitude and (1/160 Hz) frequency is given in Fig. 10.

In the cyclic voltammetry test, the voltage is controlled to vary in a triangular manner with a given frequency and amplitude, and the resulting current is measured and recorded.
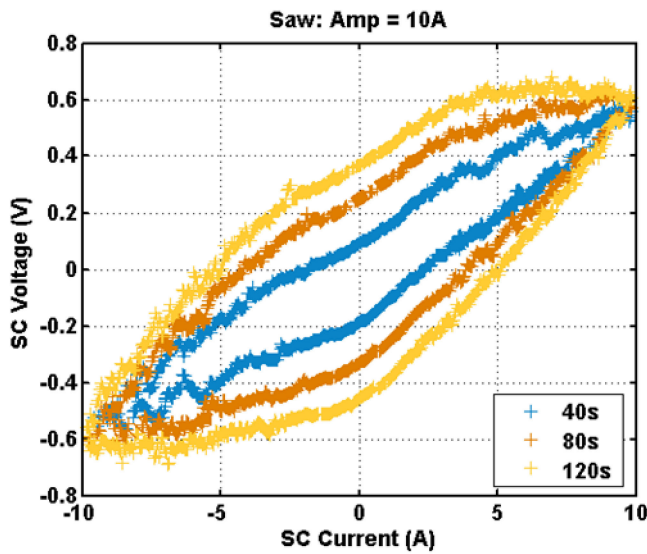
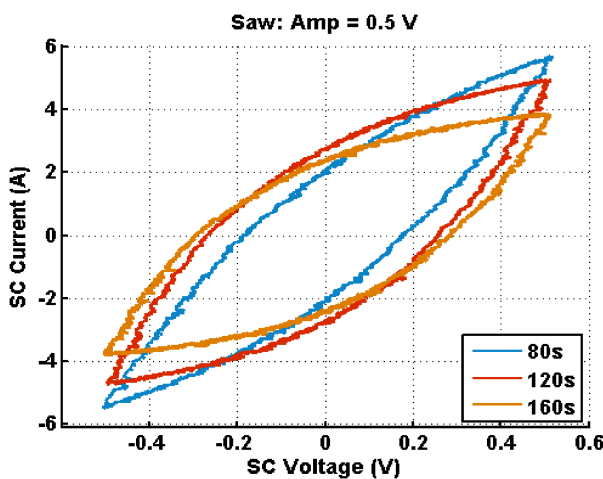**FIGURE 3.** Cyclic chrono-potentiometry test, 10 A, 1/40 Hz, 1/80 Hz, and 1/120 H$_Z$.

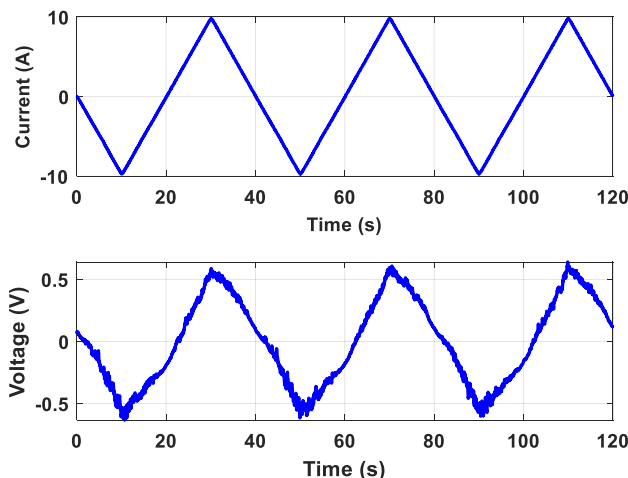**FIGURE 4.** Cyclic voltammetry test, 1 V, 1/80 Hz, 1/120 Hz, and 1/160 Hz.

FIGURE 5. Current and voltage vs. time for the curve labeled 40 s in Fig. 3.

Fig. 4, shows the I-V characteristics for a constant voltage amplitude and three different sweep rates.

For the cyclic voltammetry test, the setup used is similar to Fig. 1(a), with the difference that the hysteresis controller uses the difference between the SC voltage and the reference voltage to regulate the duty cycle. The chrono-potentiometry I-V curves show a more rounded shape compared to the voltammogram. However, with increasing scan rate, the voltammograms become increasingly biconvex due to the inability of the slow fraction of capacitive states to keep up with the applied voltage rate of change. Note that the experimental data has unipolar voltages and bipolar currents. However, the voltage waveforms shown in Figs. 3 and 4 have been centered around zero by removing their average values. This is done to highlight mainly the I-V hysteresis characteristics. As for the measured current, the sign is positive when the capacitor is charging and it is negative when discharging. Also, in our analysis and results throughout the paper, the supercapacitor was subjected to cyclic voltammetry and amperometry tests without fully discharging after each test. The objective of this was to observe the hysteresis I-V characteristics. This confirms that the voltage and current depend on their history and the different cycles they went through. The voltage and current curves in Figs. 3 and 4 show noisy signals because of the hysteresis controllers. As illustrated in Fig. 1(b), the hysteresis controller generates a variable switching frequency, which depends on the hysteresis band and the values of the current reference and capacitor voltage values, which are changing as a function of time. The capacitor voltage dynamics are normally slower than the current dynamics. Therefore, for voltage control, the PWM frequency is expected to be lower. For the given application, selecting a hysteresis band $\Delta i = 0.1$ A for the current controller and $\Delta v = 0.1$ V for the voltage controller resulted in a similar PWM frequency range of 125–500 Hz. The voltage and current signals shown in Fig. 3 and Fig. 4 have been filtered using a first-order low pass filter with a 1-Hz cut-off frequency.

III. PARAMETERS IDENTIFICATION USING VOLTAGE AND CURRENT STEP AND RAMP RESPONSE

In this section analytic expressions are derived for cyclic chrono-potentiometry of the SC module, and these expressions are used to identify the parameters of the equivalent model. The proposed approach allows calculating the model parameters using two methods: a direct identification method based on the current step and ramp excitation tests (the first method presented in Section III–A), and an adaptive online identification technique (the second method presented in Section IV). It is proposed to use an RC ladder network model to represent the SC as shown in Fig. 6. In a physical sense [7], the different time constants of the different branches of the RC ladder network in Fig. 6 model the effects of charge transmission through a supercapacitor's internal porous structure. Also, in addition to modeling the hysteresis effect in supercapacitors as visible from the I-V curves reported in the paper, the RC ladder network structure has the following
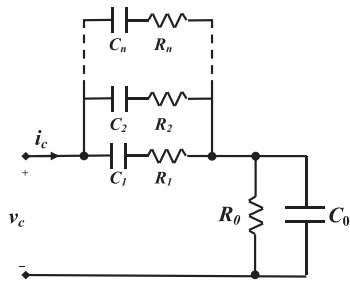
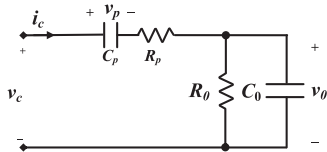**FIGURE 6.** RC ladder network model of a supercapacitor.

FIGURE 7. Reduced order RC circuit model.

advantages. Such ladder networks are widely used to approximate fractional order transfer functions and operators [25], this is because RC-ladder networks can be used to implement the mathematical process of continued fraction expansions [27] which are directly used to implement approximations of fractional order operators. So although the simple model proposed in this paper does not explicitly use fractional order calculus, but using the RC-ladder network approximation of the model provides benefits associated with fractional order models. The parallel resistance and capacitance branch in Fig. 6, Fig. 7 [7] models the effects of the bulk electrolyte (solid/liquid), and the dielectric polarization in the SC.

A. REDUCED-ORDER MODEL EQUATIONS

For parameter identification (by the first method proposed in this paper), the SC module is represented by a reduced order model as shown in Fig. 7, where the RC ladder network is replaced by one equivalent RC branch. This aids parameter identification, as mentioned in the introduction. The series resistance and capacitance branch in Fig. 7 represents the overall impedance of the RC ladder network shown in Fig. 6. Next, the equivalent model parameters are estimated using the voltage step response and the current ramp response data. Figs. 8, 9 and 10 show the voltage and current step and ramp responses of the SC module.

The equations governing the reduced order model circuit depicted in Fig. 7 can be written as:

$$i_c = C_p \frac{dv_p}{dt} \tag{1}$$

$$i_c = \frac{v_0}{R_0} + C_0 \frac{dv_0}{dt} \tag{2}$$

$$v_c = R_p i_c + v_p + v_0$$

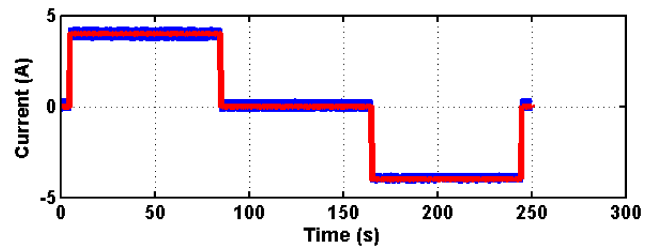$$Z_c = R_p + \frac{1}{C_p s} + \frac{R_0}{R_0 C_0 s + 1} \tag{3}$$

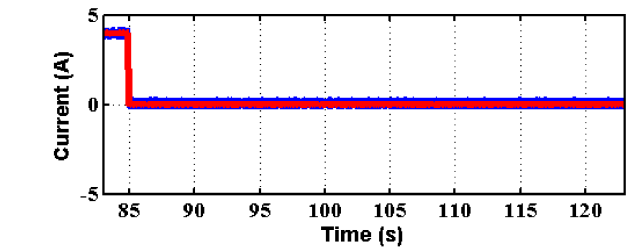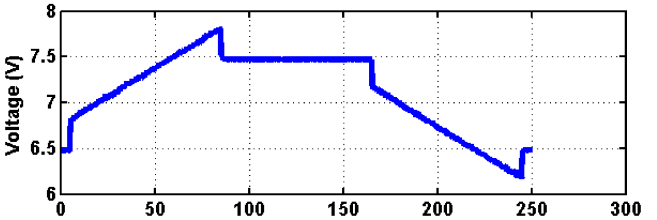**FIGURE 8.** Supercapacitor step response with hysteresis current control.

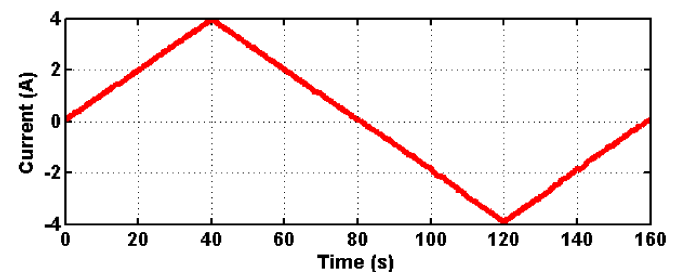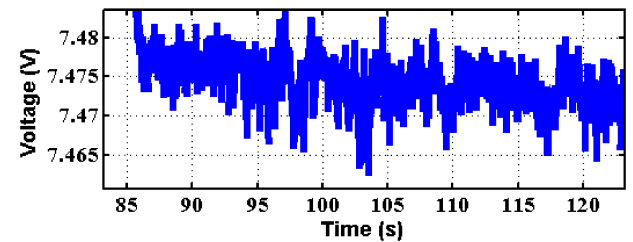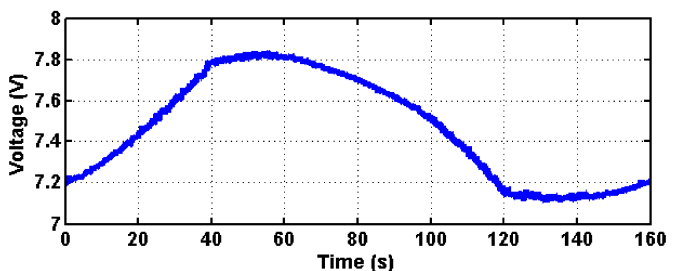**FIGURE 9.** Zoomed supercapacitor step response shows slow voltage decline.

FIGURE 10. Supercapacitor ramp response with hysteresis current control.

Step response:

$$i_c(t) = A \tag{4}$$

$$v_c(t) = A\left[R_p + R_0 + \frac{1}{C_p}t - R_0 e^{-\frac{t}{R_0 C_0}}\right] \tag{5}$$

Ramp response:

$$i_c(t) = Kt \tag{6}$$

$$v_c(t) = K\left[-R_0^2 C_0 + (R_0 + R_p)t + \frac{1}{2C_p}t^2 + R_0^2 C_0 e^{-\frac{t}{R_0 C_0}}\right] \tag{7}$$

B. PARAMETERS IDENTIFICATION OF THE REDUCED-ORDER MODEL

It can be observed from the step response equations (4) and (5) and Figs. 8, 9 and 10 that the step changes in voltage and current are directly related to the equivalent resistance R_p.

$$\begin{cases} \Delta I = i_c(0) = A \\ \Delta V = v_c(0) = A R_p \end{cases} \tag{8}$$

Therefore, R_p can be directly obtained from the step response measurements as follows.

$$R_p = \frac{\Delta V}{\Delta I} \tag{9}$$

Next, the remaining parameters (R_0, C_0, C_p) can be estimated using the ramp response data given by equation (7). Assume that the applied current is a periodic triangular waveform with a slope K and period T. The resulting ramp response $v_c(t)$ is a function of the independent variable t and the vector of n parameters $p(R_0, C_0, C_p)$. This function is fitted to a set of m measured data points (t_i, y_i) by minimizing the sum of the weighted squares of errors between the measured data $y(t_i)$ and the curve-fit function $\hat{y}(t_i, p)$ using the Levenberg-Marquardt method (LM) [29]–[32]. The LM algorithm adaptively varies the parameter updates between the Gradient Descent update and the Gauss-Newton update. The scalar-valued goodness-of-fit is called the chi-squared error criterion, and is given as,

$$\chi^2(p) = \sum_{i=1}^{m}\left[\frac{y(t_i) - \hat{y}(t_i, p)}{w_i}\right]^2, \quad .i.e. \tag{}$$

$$\chi^2(p) = y^T W y - 2y^T W \hat{y} + \hat{y}^T W \hat{y}. \tag{10}$$

The value w_i is a measure of the error in measurement $y(t_i)$. The weighting matrix W is diagonal with $W_{ii} = \frac{1}{w_i^2}$. Since the function $\hat{y}$ is nonlinear in the model parameters p so the minimization of χ^2 with respect to the parameters is carried out iteratively. The goal of each iteration is to minimize the gradient of the chi-squared objective function by finding a perturbation h to the parameters p that reduces χ^2. After taking the derivative of the chi-squared objective function, the perturbation h_{lm} where the subscript lm indicates the

(a)

(b)
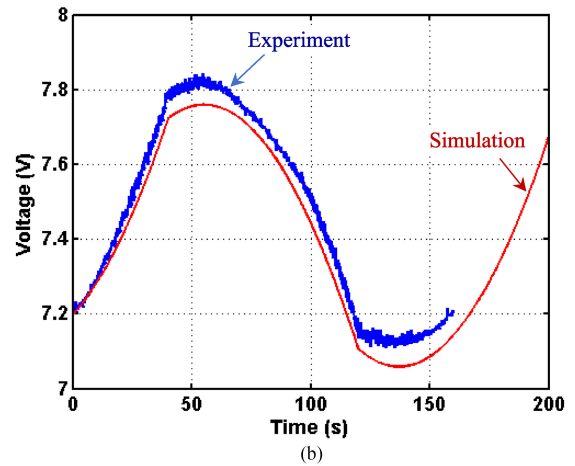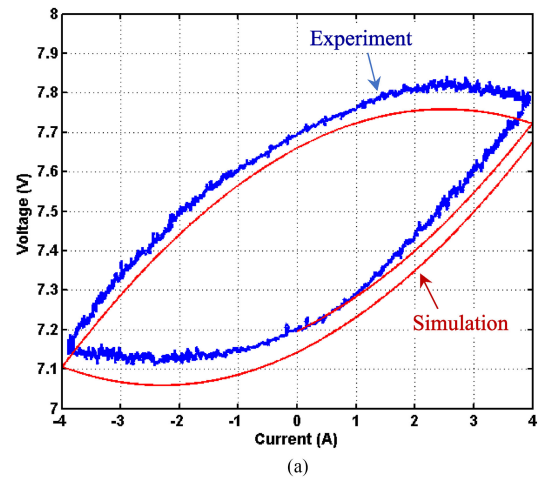
FIGURE 11. (a) Experimental hysteresis loop and simulated loop using the reduced order model. **(b)** Experimental and simulated terminal voltage plots vs time for the hysteresis loop shown in Fig. 11(a), using the reduced order model.

use of the well-known Levenberg-Marquardt algorithm that adaptively varies the parameter updates between the gradient descent update and the Gauss-Newton update, is provided by the following equation, where $J = \frac{\partial \hat{y}(p)}{\partial p}$.

$$\left[J^T W J + \lambda I\right]h_{lm} = J^T W (y - \hat{y}(p)) \tag{11}$$

In (11), small values of the algorithmic parameter λ result in a Gauss-Newton update and large values of λ result in a gradient descent update. The parameter λ is initialized to be large so that first updates are small steps in the steepest-descent direction. If an iteration happens to result in a worse approximation, λ is increased. As the solution improves, λ is decreased, the Levenberg-Marquardt method approaches the Gauss-Newton method, and the solution typically accelerates to the local minimum.

The plots depicted in Fig. 11(a), 11(b) provide comparisons between the cyclic voltammogram obtained from the commercial supercapacitor and from its equivalent model. The estimated parameters are listed in Table 1.

Symbol	Quantity	Estimated Value
R_p	equivalent series resistance	0.085 Ω
C_p	equivalent series capacitance	675.0897 F
R_0	parallel resistance	0.4788 Ω
C_0	parallel capacitance	616.9968 F

IV. ADAPTIVE PARAMETERS ESTIMATION

This section, first presents the details related to a simplified version of a supercapacitor model (as shown in Fig. 7), and also details related to an adaptive observer. Then a UAS and optimization (UAS+O) based technique to estimate the parameters of the model in Fig. 7 (the second supercapacitor parameter estimation method developed in this paper), is presented. Further using the parameters obtained from the UAS+O based technique, optimization techniques are used again to estimate parameters of the RC ladder network model of a Supercapacitor (shown in Fig. 6).

A. STATE-SPACE DESCRIPTION OF SIMPLIFIED SUPERCAPACITOR MODEL

Let states x_1, x_2 represent the voltages across the capacitors C_p, and C_0 respectively. By the sign convention used in Fig. 10, x_1, x_2 are non-negative real numbers. Let $u(t)$ represent the supercapacitor current $i_c(t)$, and $y(t)$ be the supercapacitor terminal voltage $V_c(t)$. The following equations provide an input-output dynamic model for the reduced order RC circuit representation of the supercapacitor shown in Fig. 7.

$$\dot{x}_1 = \frac{u(t)}{C_p} \tag{12}$$

$$\dot{x}_2 = -\frac{x_2}{C_0 R_0} + \frac{u(t)}{C_0} \tag{13}$$

$$y(t) = y_{off} + x_1(t) + x_2(t) + R_p u(t) \tag{14}$$

The term y_{off} represents the initial voltage (i.e., V_0) across the supercapacitor terminals.

B. ADAPTIVE OBSERVER

An objective of this paper is to estimate the values of the constants R_p, C_p, R_0, C_0 used in the supercapacitor model (1)–(3). Let $\hat{a}_1(t)$, $\hat{a}_2(t)$, $\hat{a}_3(t)$, $\hat{a}_4(t)$ represent the estimated values of the constants R_p, C_p, R_0, C_0 respectively. The following adaptive observer is used to obtain the required values of $\hat{a}_1(t)$, $\hat{a}_2(t)$, $\hat{a}_3(t)$, $\hat{a}_4(t)$.

$$\dot{\hat{x}}_1 = \frac{u(t)}{\hat{a}_2(t)} + u_a(t), \ \hat{x}_1 \geq 0 \tag{15}$$

$$\dot{\hat{x}}_2 = -\frac{\hat{x}_2(t)}{\hat{a}_4(t)\hat{a}_3(t)} + \frac{u(t)}{\hat{a}_4(t)} + u_a(t), \ \hat{x}_2 \geq 0 \tag{16}$$

$$\hat{y}(t) = y_{off} + \hat{x}_1(t) + \hat{x}_2(t) + \hat{a}_1(t)u(t) \tag{17}$$

In (15)–(17) the variables $\hat{x}_1$, $\hat{x}_2$, $\hat{y}$ represent estimates of the states x_1, x_2 in (12)–(14) and the terminal voltage y respectively. In accordance with the signs of x_1, x_2, the estimated states $\hat{x}_1$, $\hat{x}_2$ are non-negative real numbers, this can be easily enforced by using a saturation with lower limit of zero w.r.t. $\hat{x}_1$, $\hat{x}_2$. The terms $u(t)$ and y_{off} represent the supercapacitor current $i_c(t)$, and the initial supercapacitor terminal voltage in (15)–(17). The input to the adaptive observer is represented by the term $u_a(t)$ and is defined below:

$$u_a(t) = -N(k(t))e(t), \quad \text{where} \tag{18}$$

$$\dot{k}(t) = e^2(t), \ k(t_0) > 0 \tag{19}$$

$$e(t) = y(t) - \hat{y}(t), \tag{20}$$

$$N(k(t)) = E_\alpha\left(-\lambda k(t)^\alpha\right), \quad \lambda > 0, \quad \alpha \in (2,3). \tag{21}$$

The switching function $N(\cdot)$ is known as a Nussbaum function, which is defined as follows.

Definition: Let $k' \in \mathbb{R}$. A piecewise right continuous and locally Lipschitz function $N(\cdot): [k' \to \mathbb{R}]$ is a Nussbaum function if it satisfies $\underset{k > k_0}{sup} \ \frac{1}{k-k_0}\int_{k_0}^k N(\tau)d\tau = +\infty$ and, $\underset{k > k_0}{inf} \ \frac{1}{k-k_0}\int_{k_0}^k N(\tau)d\tau = -\infty$.

Switching functions of Nussbaum type are very common in UAS based systems [22]–[24], [33]. For this work, we use a Nussbaum function of Mittag-Leffler (ML) form $E_\alpha(z)$, which is given by

$$E_\alpha(z) = \sum_{k=0}^{\infty} \frac{z^k}{\Gamma(k\alpha + 1)}, \tag{22}$$

where the function $\Gamma(z+1) = z\Gamma(z), z > 0$ is the standard Gamma function, and α is a parameter. It is known from the literature that $E_\alpha(-\lambda t^\alpha)$, is a Nussbaum function for $\lambda > 0$, $\alpha \in (2,3)$ [34]. A Nussbaum function of ML form is chosen for this work, because earlier efforts in [35] have shown that Nussbaum functions of ML form provide very fast error convergence, and reasonable robustness to disturbances and noise.

Now consider the following equations used for updating the values of the parameters $\hat{a}_1(t)$, $\hat{a}_2(t)$, $\hat{a}_3(t)$, $\hat{a}_4(t)$ adaptively,

$$\dot{\hat{a}}_n(t) = e^2(t) + \lambda_{xn}(a_{nu} - \hat{a}_n(t)) + \lambda_{yn}(a_{nl} - \hat{a}_n(t)) \tag{23}$$

where $\hat{a}_n(t) \in \mathbb{R}$, and $n \in \{1, \ldots, 4\}$. In (23) $a_{nu}, a_{nl} \in \mathbb{R}_{\geq 0}$ represent upper and lower bounds respectively on the steady state of a parameter value $\hat{a}_n$. Similarly, the non-negative weights $\lambda_{xn}, \lambda_{yn} \in \mathbb{R}_{\geq 0}$ represent a user's confidence in the chosen upper and lower bounds a_{nu}, a_{nl} respectively.

C. SUPERCAPACITOR PARAMETER ESTIMATION ALGORITHM

The following points illustrate the steps of the proposed supercapacitor parameter estimation algorithm, as shown in Fig. 12.
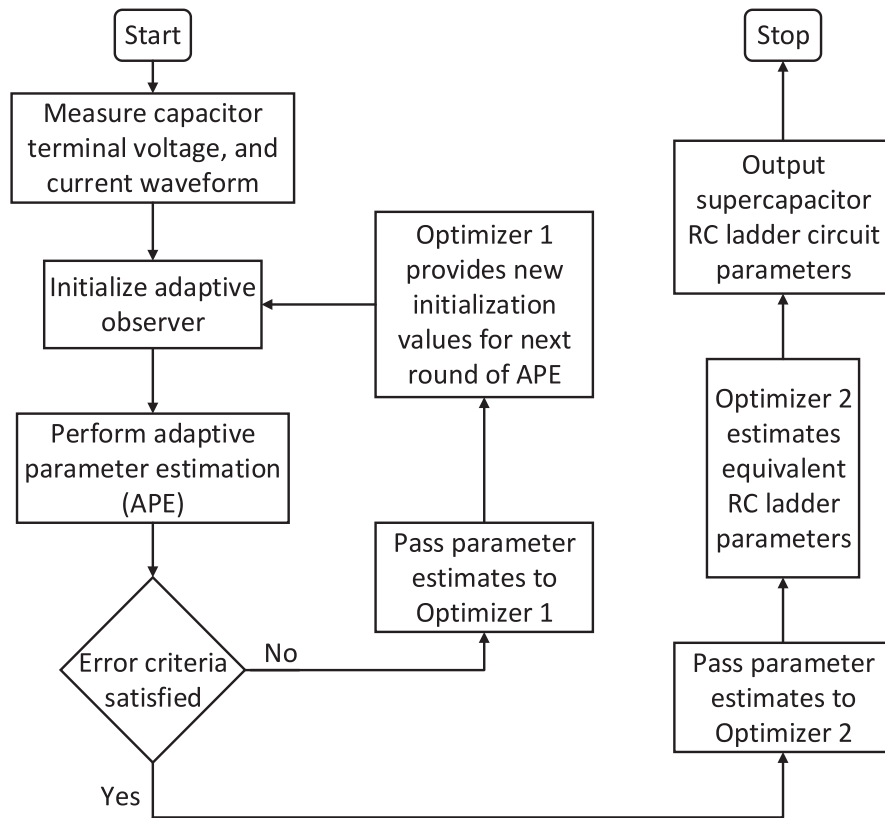 1) The process starts with the measurement of supercapacitor current, and voltage waveforms. After this is

FIGURE 12. Method proposed for supercapacitor parameters estimation.

done, the adaptive observer is initialized. The adaptive observer requires the following inputs: supercapacitor current $i_c(t)$, supercapacitor terminal voltage $v_c(t)$, initial offset voltage y_{off}, initial conditions $k(t_0)$ for the adaptive gain $k(\cdot)$, initial conditions for the supercapacitor parameters being estimated i.e., $\hat{a}_n(t_0)$, $n \in \{1, \ldots, 4\}$, steady-state upper and lower bounds on estimated parameter values i.e., a_{nu}, a_{nl} respectively for $n \in \{1, \ldots, 4\}$, and weights $\lambda_{xn}, \lambda_{yn}$ for $n \in [1, \ldots, 4]$. At the start of the proposed parameter estimation algorithm, all the above values are required to be provided by a user, in subsequent iterations, the above values are provided by an optimizer block. At every time instant, the APE in Fig. 12 integrates (23) to find $\hat{a}_n(t)$, $n \in \{1, \cdots, 4\}$, then it computes $u_a(t)$ and propagates the observer equations forward to get estimated values of $\hat{x}_1$, $\hat{x}_2$, $\hat{y}$ at the next time step. This process continues until samples are available for $i_c(t)$, $v_c(t)$ for time $t \in [t_0, T]$, here t_0 is the initial time instant at which current and voltage measurements were started, and T represents the last time instant for which recorded current and voltage measurements are available. At the end of the above mentioned adaptive parameter estimation process, the APE produces estimated values $\hat{R}_0$, $\hat{C}_0$, $\hat{R}_p$, $\hat{C}_p$. Once the APE terminates, the error criteria $\sum_{t=t_0}^{t=T} (v_c(t) - \hat{y}(t))^2$ is used to check if the difference between the terminal voltage estimated by

the APE, and the actual terminal voltage is smaller than a user specified threshold value. If the threshold is not satisfied, it means that the initial values fed to the APE can be optimized, so the estimated parameters $\hat{R}_0$, $\hat{C}_0$, $\hat{R}_p$, $\hat{C}_p$ are fed to the 'Optimizer 1' block.

2) This block tries to minimize the error between the terminal voltage measured and estimated by the APE by using the following objective function.

$$J_1 = \sum_{t=t_0}^{t=T} (v_c(t) - \hat{y}(t))^2. \tag{24}$$

The 'Optimizer 1' block performs its own internal iterations and outputs updated values of $k(t_0)$, $\hat{a}_n(t_0)$, $a_{nu}, a_{nl}, \lambda_{xn}$, and λ_{yn}, for $n \in \{1, \ldots, 4\}$ to be utilized in the next iteration of the APE, so that the objective function J_1 in (24) is minimized. For this work, we have used the standard constrained optimization routine 'fmincon' available in MATLAB's optimization toolbox. This entire process of adaptive parameter estimation followed by adjusting the values of $k(t_0)$, $\hat{a}_n(t_0)$, a_{nu}, a_{nl}, λ_{xn}, and λ_{yn} using an optimization routine constitutes one iteration of our proposed UAS+O based algorithm for supercapacitor parameters estimation. The UAS+O iterations continue until the objective function falls below a certain user

specified small threshold value, smaller threshold values yielding better results.

3) Once the UAS+O iterations terminate (i.e., the error criteria $\sum_{t=t_0}^{t=T} (v_c(t) - \hat{y}(t))^2$ is below a user specified small threshold value), then optimal estimates of $\hat{R}_0$, $\hat{C}_0$, $\hat{R}_p$, $\hat{C}_p$ are available. These optimal estimates of $\hat{R}_0$, $\hat{C}_0$, $\hat{R}_p$, $\hat{C}_p$ are then fed into a second optimization block 'Optimizer 2' shown in Fig. 12 to approximate the series combination of $\hat{R}_p$, $\hat{C}_p$ using a three-rung ladder network consisting or R_1, C_1, R_2, C_2, and R_3, C_3. This block requires the bandwidth $[w_l, \ldots, w_h]$, the number N of frequency steps over which the three-rung ladder network is required to approximate the series combination of $\hat{R}_p$, $\hat{C}_p$, and constraints related to the R_1C_1, R_2C_2, and R_3C_3 time constants which are desired to be satisfied. The objective function used for this optimization block is,

$$J_2 = \left(\frac{w_h - w_l}{N}\right) \sum_{w=w_l}^{w=w_h} \left(Z_p(w) - Z_{eq}(w)\right)^2, \text{ where}$$

(25)

$$Z_p(w) = \left|\hat{R}_p + \frac{1}{jw_{\hat{C}_p}}\right|, \ w \in \{w_1, w_2, \ldots, w_k, \ldots, w_N\}$$

(26)

$$Z_{eq}(w) = \frac{1}{\left(Z_1^{-1}(w) + Z_2^{-1}(w) + Z_3^{-1}(w)\right)},$$

(27)

in the above $Z_i = R_i + jX_{C_i}$, with $i \in \{1, 2, 3\}$, and $X_{C_i} = \frac{1}{jwC_i}$, where $w \in \{w_1, w_2, \ldots, w_k, \ldots, w_N\}$ with $w_1 = w_l$, $w_N = w_h$, and $w_{k+1} - w_k = \frac{w_h - w_l}{N}$, $k \in \{1, \ldots, N-1\}$. The equality constraints $\tau_1 = R_1C_1$, $\tau_2 = R_2C_2$, $\tau_3 = R_3C_3$ and the inequality constraints $R_1C_1 + \epsilon_1 \le \alpha_2\tau_2$, $R_2C_2 + \epsilon_2 \le \alpha_3\tau_3$, $R_1C_1 + \epsilon_3 \le \alpha_1\tau_3$ were also used to guarantee that the three-rung approximation of the series combination of $\hat{R}_p, \hat{C}_p$ resulted in distinct resistor and capacitor values with three distinct time constants. The small positive numbers $\epsilon_1 \ne \epsilon_2 \ne \epsilon_3$ are required for using MATLAB's 'fmincon' optimization routine to implement strict inequality constraints. Also, by experimentation α_1, α_2, α_3 are chosen as 20, 2, 10. It is also worth mentioning that in our implementation, the time constants τ_1, τ_2, τ_3 are iteratively chosen by the optimizer, and are not prespecified. The initial guesses for every resistor and capacitor value are set to zero, the initial guesses for τ_1, τ_2, τ_3 are set as 50, 100, and 1000 respectively. Also, the lower, and upper bounds for all resistor and capacitor values are set to zero, and infinity respectively. The lower and upper bounds for the time constants τ_1, τ_2, τ_3 are set to 30, 80, 700 and 70, 130, 1500 respectively.

D. MATHEMATICAL DETAILS OF ADAPTIVE PARAMETER ESTIMATION

The following result establishes the positivity of the parameters $\hat{a}_n(t)$ in (23). This result is required to prove that the error $e(t)$ converges to zero with time.

Lemma 4.D.1: Suppose $a_{nu}, a_{nl}, \lambda_{xn}$, and λ_{yn} are nonnegative real numbers, and let $\hat{a}_n(t)$ be defined as in (23). If $\hat{a}_n(t_0) > 0$, then $\hat{a}_n(t) > 0$ for all time $t \in [t_0, \infty)$ for all $n \in \{1, \ldots, 4\}$.

Proof: Please see Appendix A. □

The following result uses the positivity of $\hat{a}_n(t)$ from the above Lemma 4.D.1. and shows that $e(t) \to 0$ as $t \to \infty$.

This is required to show that the adaptive observer in (15)-(17) can be used to estimate supercapacitor model parameters.

Theorem 4.D.2: Let $e(t)$ be as defined in (20), and assume that there exists a time instant T such that $u(t) \to 0$, $\dot{u}(t) \to 0$, and $\dot{y}(t) \to 0$ for all time $t > T$. If the conditions required for Lemma 4.D.1 to hold are satisfied, then $e(t) \to 0$ as $t \to \infty$.

Proof: Please see Appendix B. □

By using the above result, the following theorem shows that the proposed adaptive estimation scheme makes the parameters $\hat{a}_1(t)$, $\hat{a}_2(t)$, $\hat{a}_3(t)$, $\hat{a}_4(t)$ converge to the values of the constants R_p, C_p, R_0 and C_0 respectively. First certain vectors used in the next result are defined.

$$\text{Let: } \bar{v}_1(t) = [\,1 \quad 1 \quad u(t)\,], \bar{v}_2(t) = \begin{bmatrix} x_1(t) - \hat{x}_1(t) \\ x_2(t) - \hat{x}_2(t) \\ R_p - \hat{a}_1(t) \end{bmatrix},$$

and

$$\text{let } \bar{v}_3(t) = [\,x_2(t) \quad u(t)\,], \bar{v}_4(t) = \begin{bmatrix} (\frac{1}{C_0R_0} - \frac{1}{\hat{a}_4(t)\hat{a}_3(t)}) \\ (\frac{1}{\hat{a}_4(t)} - \frac{1}{C_0}) \end{bmatrix}.$$

Now consider the statement of the following result.

Theorem 4.D.3: Let $\hat{a}_1(t)$, $\hat{a}_2(t)$, $\hat{a}_3(t)$, $\hat{a}_4(t)$ represent the estimated values of the constants R_p, C_p, R_0, C_0 respectively. Let $e(t)$ be as defined in (20). Assuming $x_2(t) \ne 0$, if there exists a time instant T such that $u(t) \to 0$, $u(t) \ne 0$, $\dot{u}(t) \to 0$, $\dot{y}(t) \to 0$, and $\bar{v}_2(t)$, $\bar{v}_4(t)$ are not in the null spaces of $\bar{v}_1(t)$, $\bar{v}_3(t)$ respectively for all time $t > T$, then $\hat{a}_1(t) \to R_p, \hat{a}_2(t) \to C_p, \hat{a}_3(t) \to R_0, \hat{a}_4(t) \to C_0$ as $t \to \infty$.

Proof: Please see Appendix C. □

Note that the assumptions $x_2(t) \ne 0$, $u(t) \to 0$, and $u(t) \ne 0$, $\dot{u}(t) \to 0$, are reasonable. This is because x_2 represents the voltage across the capacitance C_0, usually it is time-consuming to get the residual voltage in a supercapacitor to zero, therefore this assumption removes the necessity of zero residual voltage. Further $u(t) \to 0$, and $u(t) \ne 0$, $\dot{u}(t) \to 0$ simply means that for the parameters estimation to be accurate, the supercapacitor current should tend to zero but not identically zero, and this should happen in a somewhat smooth manner i.e., $\dot{u}(t) \to 0$. This assumption is not hard to meet either, because connecting a DC voltage source across a supercapacitor for charging it, or discharging a supercapacitor through a resistive load, will result in current waveforms which meet the above assumptions as the supercapacitor nears its fully charged/discharged state.

TABLE 2. Adaptively Estimated Parameters of the Reduced-Order Model

Symbol	Quantity	Estimated Value
R_p	Equivalent series resistance	$\hat{R}_p = 0.0576\ \Omega$
C_p	Equivalent series capacitance	$\hat{C}_p = 642.848$ F
R_0	Parallel resistance	$\hat{R}_0 = 0.2978\ \Omega$
C_0	Parallel capacitance	$\hat{C}_0 = 577.593$ F

TABLE 3. Estimated Parameters of the Ladder Network

| Symbol	Quantity	Estimated Value
R_1	Ladder rung 1 resistance	0.0921 Ω
C_1	Ladder rung 1 capacitance	326.0591 F
R_2	Ladder rung 2 resistance	0.1664 Ω
C_2	Ladder rung 2 capacitance	480.9689 F
R_3	Ladder rung 3 resistance	2.1107 Ω
C_3	Ladder rung 3 capacitance	387.829 F

V. EXPERIMENTAL RESULTS FOR ADAPTIVE PARAMETERS ESTIMATION

In this section the results of the proposed UAS+O based supercapacitor parameter estimation scheme are presented. The supercapacitor module used is a 15V UC bank, consisting of six DLCAP Supercapacitors from NIPPON CHEMI-CON connected in series. Each capacitor has a rating of 2.5V, 2300F. The parameters for the model shown in Fig. 7 are first estimated using the UAS+O approach with experimental data. The results obtained are shown in Table 2. The experimental data used for obtaining the estimated parameters $\hat{R}_0$, $\hat{C}_0$, $\hat{R}_p$, $\hat{C}_p$ shown in Table 2 is shown in Fig. 11. After the parameters $\hat{R}_0$, $\hat{C}_0$, $\hat{R}_p$, $\hat{C}_p$ are obtained then, the values of $\hat{R}_p$, $\hat{C}_p$ are fed into the 'Optimizer 2' block, and the parameters R_1, C_1, R_2, C_2, R_3, and C_3 are obtained as shown in Table 3. This provides a model of the form showed in Fig. 6, with (n = 3).

It should be noted that all the results shown in this section are obtained using the parameters shown in Tables 2 and 3, i.e., parameter identification was only done once on one set of experimental data, and satisfactory results are observed on testing above obtained parameters with many other sets of experimental data. For testing of the supercapacitor model parameters obtained using the UAS+O based procedure, the results shown in Tables 2 and 3 are verified with four data sets, with the supercapacitor current as the input, and the supercapacitor terminal voltage as the output. The results of the four tests whose error statistics are summarized in Table 4, are shown in Figs. 13 to 16 respectively. The details related to the terminal voltages, and the input currents for these tests shown in Table 4 are as follows: (a) Test 1: triangular wave input current with peak to peak magnitude of +/–4 A, period of 160 s, terminal voltage magnitude between 7–7.8 V (initial voltage 7.2 V) (b) Test 2: triangular wave input current with peak to peak magnitude of +/- 10A, with period of 80 s, terminal voltage magnitude between 6.2–7.4 V (initial voltage 6.25 V)

TABLE 4. Error Statistics: UAS+O Tests With I-as Input and V-as Output

Test name	Test with adaptively estimated model parameters from Table 2		Test with estimated model parameters of the equivalent RC-ladder network from Table 3	
	Average absolute error (V)	Percentage error (%)	Average absolute error (V)	Percentage error (%)
Test 1	0.0301	0.4087	0.0749	1.0179
Test 2	0.0591	0.9097	0.0447	0.6881
Test 3	0.0493	0.4967	0.1004	1.0116
Test 4	0.1328	1.1338	0.1430	1.2207
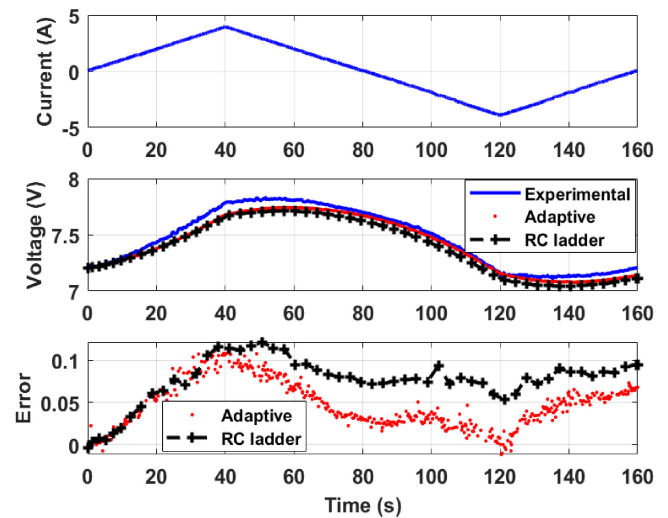
FIGURE 13. Results of Test 1 in Table 4, using UAS+O based parameter identification.

(c) Test 3: triangular wave input current with peak to peak magnitude of +/–10A, with period of 80 s, terminal voltage magnitude between 9.6–11.1V (initial voltage 9.66 V) (d) Test 4: trapezoidal input current with the following profile, −10 A from 0–14s, linear increase from −10 A to 10 A from 14–63s, flat 10 A current from 63–94 s, linear decline from 10A to −10 A from 94–142 s, and flat −10 A current from 142–160 s, terminal voltage magnitude between 11.33–13.22 V (initial voltage 11.42 V).

As visible from the numbers in Table 4, the absolute average error is very low. The percentage errors in each case are determined by taking the ratio of the average of the absolute error, the average of the estimated terminal voltage and multiplying the result by 100. The low values indicate that on average the percentage error is significantly low. Also, we can perform this calculation without significant error, because for each of the four tests, the actual supercapacitor terminal voltage has measured average values which are in the range of 7V – 12V. In the following section, we present additional results which validate the supercapacitor models proposed, and the parameters estimated by the techniques proposed in this paper.
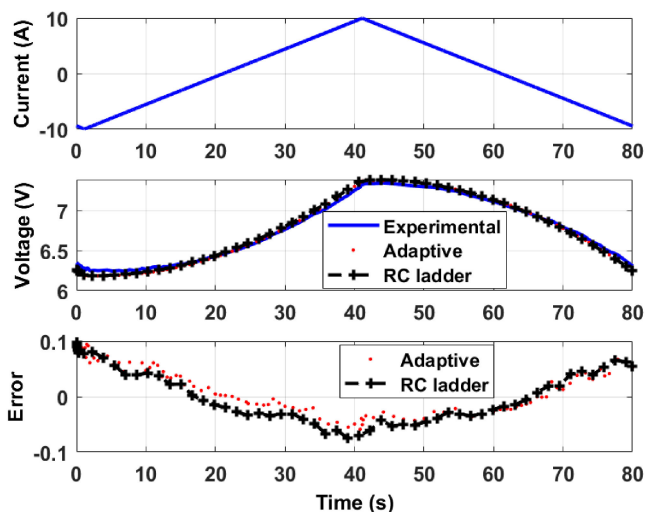
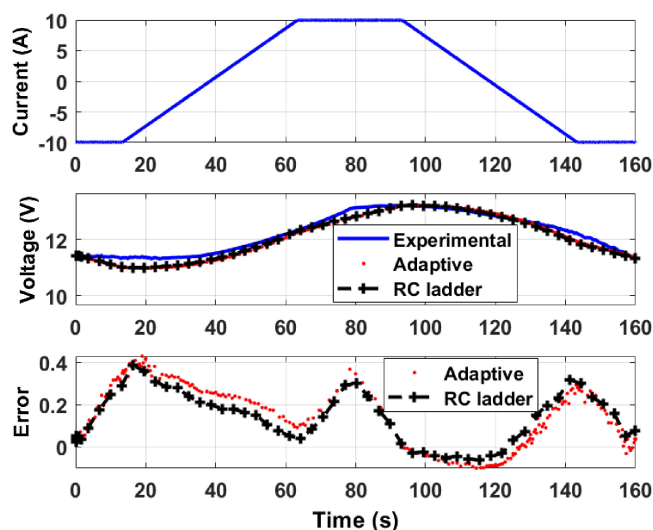**FIGURE 14.** Results of Test 2 in Table 4, using UAS+O based parameter identification.

FIGURE 16. Results of Test 4 in Table 4, using UAS+O based parameter identification.
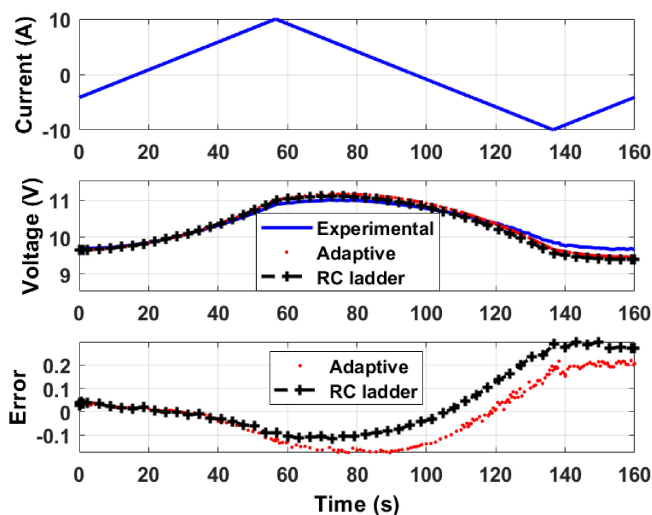

FIGURE 15. Results of Test 3 in Table 4, using UAS+O based parameter identification.
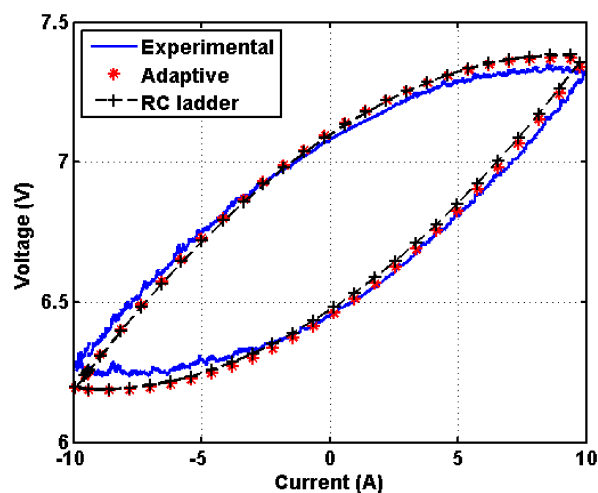

FIGURE 17. V-I curves for Test 2 in Table 4, using UAS+O based parameter identification.

VI. VALIDATION

To further analyze the results obtained and to validate the proposed SC models, and the parameter estimation techniques, we present the following data. Fig. 17 shows the V-I curves for the second test, whose data is presented in Fig. 14. It is clear from Fig. 17 that a very good match is obtained between the actual terminal voltage, and the voltage estimated by the simplified supercapacitor model whose parameters are estimated using the UAS+O technique. Similarly, the optimization procedure used to convert the above model into the three-rung RC-ladder network also provides good results as seen in Fig. 17. Fig. 18 provides the results of using the simplified model with UAS+O based parameters, and the RC- ladder equivalent model parameters from Tables 2 and 3 respectively, but with SC terminal voltage as the input and the current as output. As seen from Fig. 18 the output current estimation

error is large in the beginning, but it decreases with time. It is to be noted that the initial conditions for the current for the adaptive and RC ladder based results has been set to zero. So while it may not be possible to get detailed analysis related to the transient analysis, the steady state error in Fig. 18 settles very close to zero with time. Further Fig. 19 presents the data from Fig. 18 in the form of I-V curves. From this it is clear, that the error when estimating current with the terminal voltage as input, as presented in Fig. 18, is larger than the opposite case (i.e., current as input, terminal voltage as output as seen in Fig. 17). This is expected because the entire problem setup for the UAS+O based model parameters estimation assumes the SC current as input, terminal voltage as output. It must be noted that the error in Fig. 19 appears exaggerated due to zooming-in, although the steady state error settles to around 0.396 A around 320 s. Comparable results are obtained for
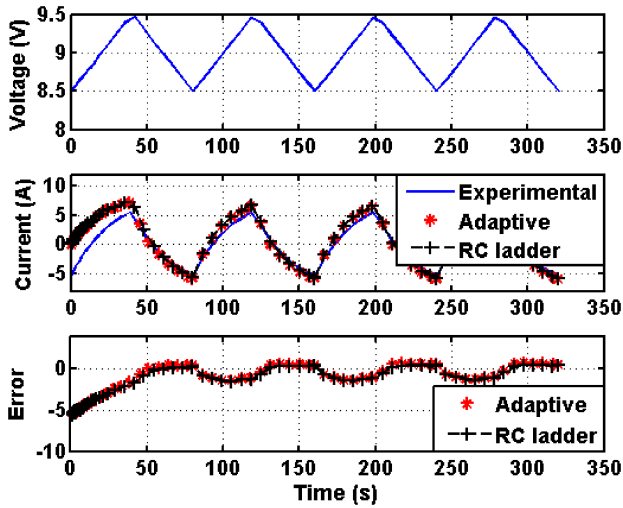
FIGURE 18. Validation of the supercapacitor model using parameters provided in Tables 2, 3 and with terminal voltage as input, and current as output.
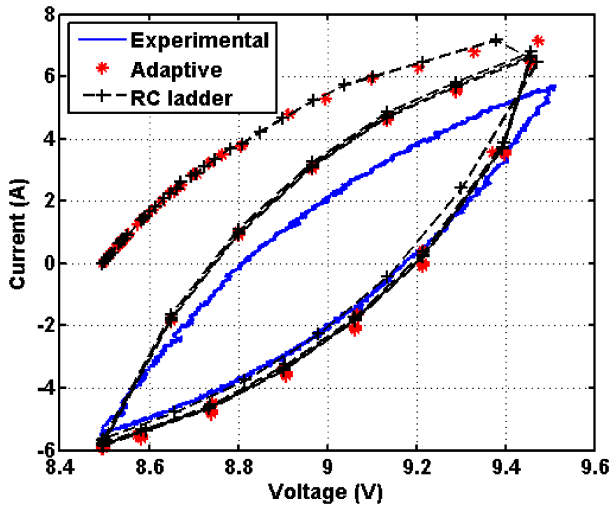

FIGURE 19. I-V curves for validation of the supercapacitor model using parameters provided in Tables 2, 3 and with terminal voltage as input, and current as output.

FIGURE 20. Bode plot of the RC ladder network model of the supercapacitor in Fig. 6 with parameter values from Table 3.

FIGURE 21. Zubieta's supercapacitor model [5].

ladder network approximation of the SC model in Fig. 7 with parameter values as given in Table 3. As is obvious, up to 10^{-2} Hz, the magnitude plot shows a decline at a rate that is not a multiple of 20 dB/decade. And also in this region up to 10^{-2} Hz the phase is approximately flat, which is further evidence of the iso-damping property common in fractional order systems, and shows that the ladder network although simple, embodies such properties related to fractional order systems.

VII. COMPARISON WITH AN EXISTING METHOD
In this section, the methodology proposed in this paper is compared with another well-known method, and an associated model for supercapacitors [5]. Zubieta's model as available in [5], is shown in Fig. 21. It consists of three parallel RC branches containing fixed resistances R_1, R_2, R_3 and fixed capacitances C_1, C_2, C_3. It also has a leakage resistance R_{leak} in parallel to the above mentioned branches, which helps model loss of charge without the presence of any load. Additionally the first branch contains a voltage dependent capacitance $C_v \times V_{ci}$ in parallel with the first branch capacitance C_1. The terminal voltage is represented by V_t, and V_{ci} is the voltage across the parallel combination of C_1 and $C_v \times V_{ci}$. The method for identifying the parameters of the model shown in Fig. 21, which is mentioned

other such tests as well. Also, the experimental data presented in Fig. 19 is the same as in Fig. 4 for the 80 s case. This is done so that the UAS+O based parameters estimation technique, and the RC-equivalent ladder network are compared with the step response, and ramp response based techniques using a similar data set. Further, comparing the parameter values shown in Tables 1, 3 shows that the values estimated for R_p, C_p, R_0, C_0 lie in the similar range of magnitude regardless of using the step, ramp response based methods, or using the UAS+O based methods. This further verifies the simplified models proposed in this paper, and verifies the associated parameters estimation techniques presented.

To validate the analogy between our proposed RC ladder network and fractional order models of supercapacitors from the literature, in Fig. 20 we show the bode plot of our RC
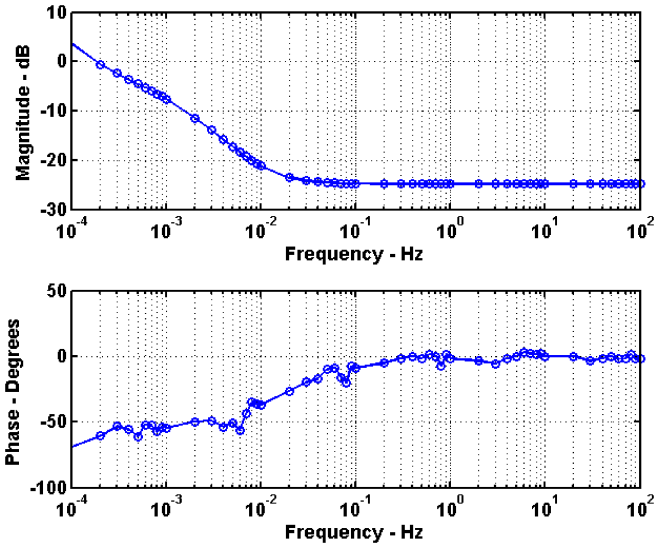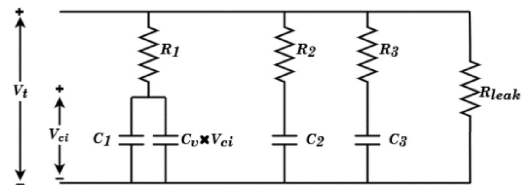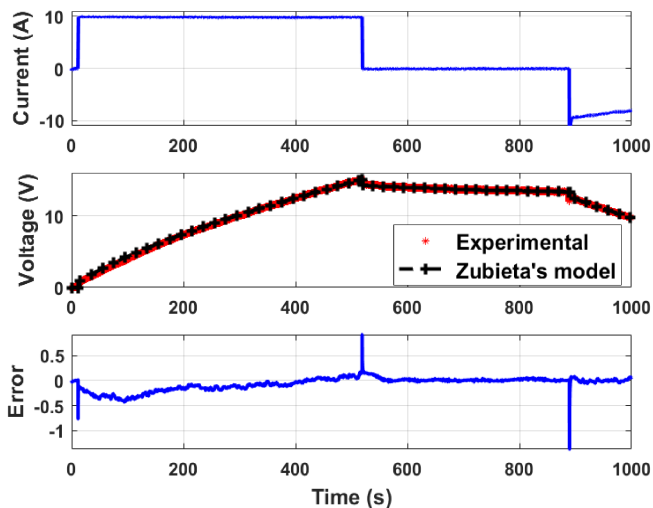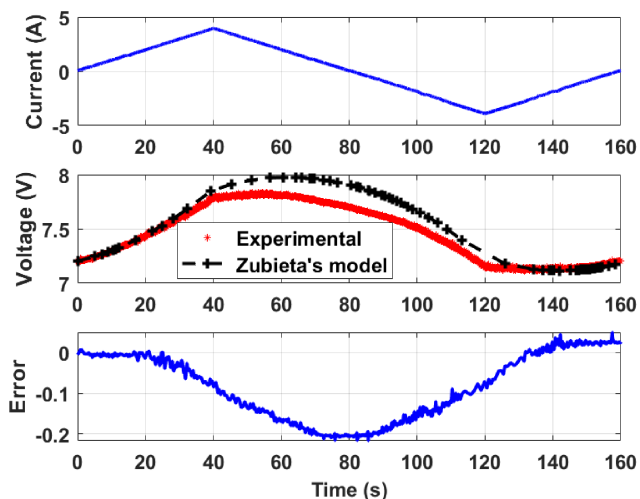
FIGURE 22. Results obtained using Zubieta's model, and manual method of supercapacitor parameters estimation from [5].

TABLE 5. Error Statistics: Tests With I-as Input and V-as Output. Data Used is the Same as Used to Get Table 4 But With Zubieta's Model and Manually Estimated Parameters as Per [5]
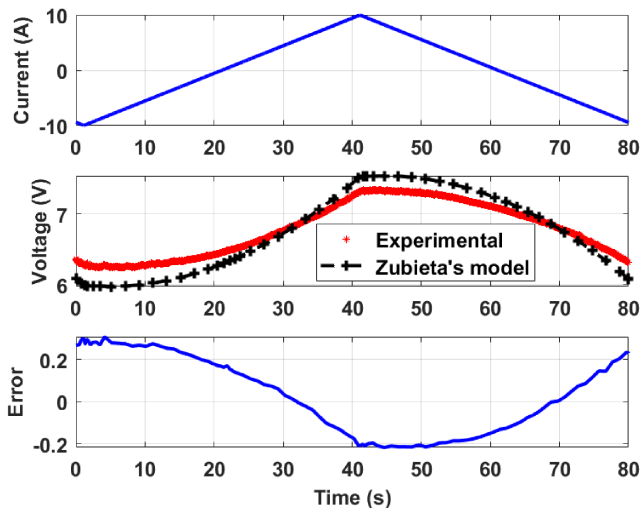
Test name	Test with Zubieta's supercapacitor model, and manual parameters estimates using the process mentioned in [5].	
	Average absolute error (V)	Percentage error (%)
Test 5	0.0985	1.3188
Test 6	0.1731	2.5531
Test 7	0.2999	2.9008
Test 8	0.3951	3.2279

in [5], requires manually identifying events in the terminal voltage waveform corresponding to a given input current. Using the setup as shown in Fig. 2, and following the procedure from [5] provides the following values for the model in Fig. 21: $R_1 = 0.0780\ \Omega$, $R_2 = 7.4363\ \Omega$, $R_3 = 7.0648\ \Omega$, $C_1 = 204\ F$, $C_2 = 37.8841\ F$, $C_3 = 68.4220\ F$, $R_{leak} = 4.8\ k\Omega$, $C_v = 13.0571\ F/V$. For details related to the process of identifying the parameters, readers are directed to [5]. The input current waveform used to identify the above mentioned parameters, and the associated voltage waveform is shown in Fig. 22. The model shown in Fig. 21 is simulated in MATLAB 2020, to get the black curve in the second panel of Fig. 22.

To compare the methods proposed for supercapacitor parameter identification in this paper vs. [5], the values of the parameters mentioned earlier in this section (Section VII), are used with the Simulink model of Fig. 21, and the output voltage error is observed; given that the inputs are the same current waveforms shown in Figs. 13–16. The results of these tests are summarized in Table 5. Figures 23–27 show the voltage, current and error plots related to the tests in Table 5. Comparing the results in Tables 4, 5 it is obvious immediately that the proposed models and the related methodologies
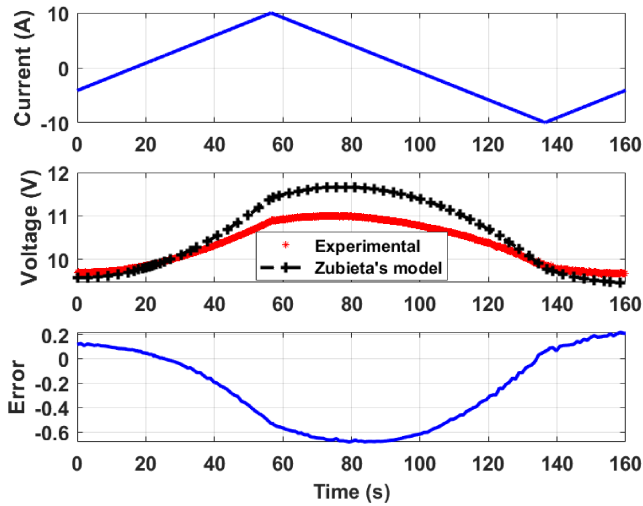

FIGURE 23. Test 5: Results obtained using parameters and the supercapacitor model by Zubieta's method [5], with the current input and voltage output data shown in Fig. 13.

FIGURE 24. Test 6: Results obtained using parameters and the supercapacitor model by Zubieta's method [5], with the current input and voltage output data shown in Fig. 14.

results in lower error. From the overall average percentage error across the four tests shown in Tables 4, 5 the following can be concluded. If the average of the absolute average percentage error is calculated for the UAS+O based approach with the simplified model shown in Fig. 7, this gives 0.7372 across the four tests shown. For the RC ladder approximation based model shown in Fig. 6, and Zubieta's model shown in Fig. 21; the average value across the four tests presented, of the absolute average percentage error is 0.9846, and 2.5002 respectively. This conclusion is very clearly seen from the bar graph in Fig. 27 comparing the results in Tables 4, 5. Also, for the reverse validation test shown in Fig. 28 with the data in Fig. 18 i.e., voltage as input and current as output, Zubieta's model has a steady state error of 2.4728 A, compared to the 0.396 A obtained with the models and methodology presented

FIGURE 25. Test 7: Results obtained using parameters and the supercapacitor model by Zubieta's method [5], with the current input and voltage output data shown in Fig. 15.
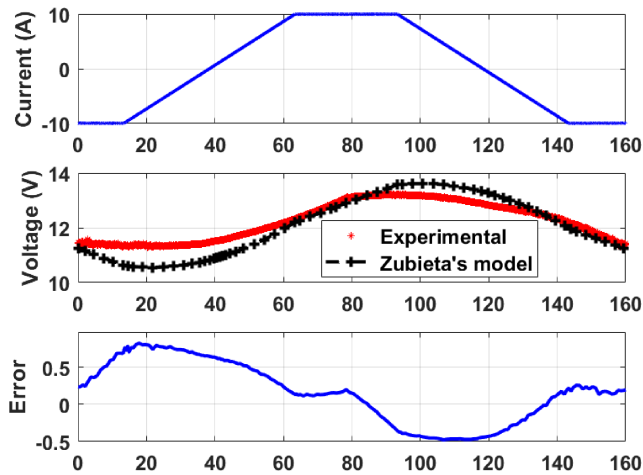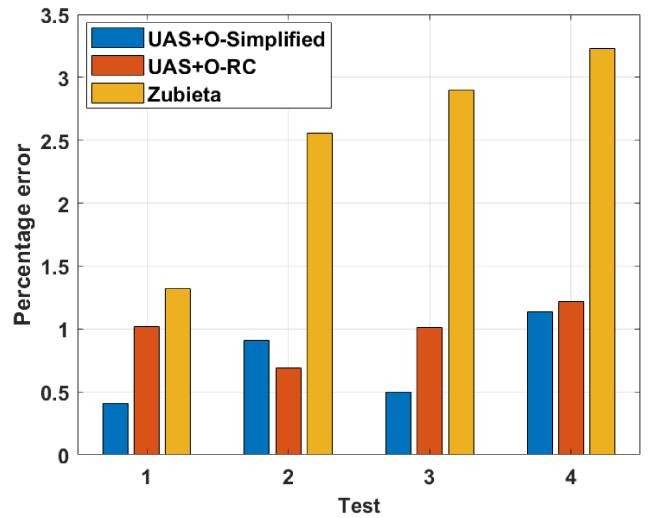

FIGURE 26. Test 8: Results obtained using parameters and the supercapacitor model by Zubieta's method [5], with the current input and voltage output data shown in Fig. 16.
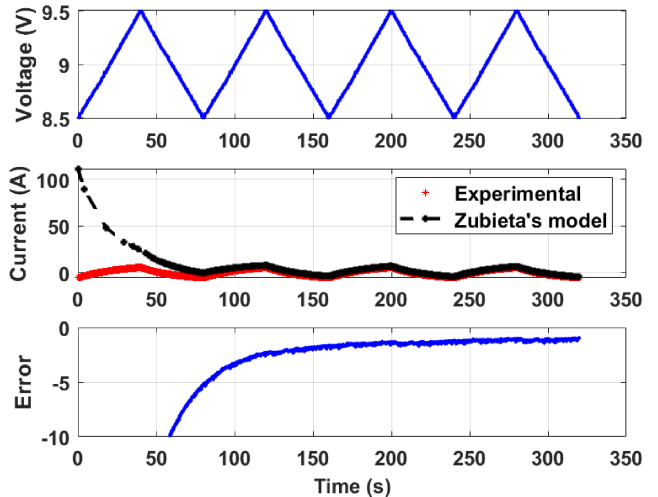

FIGURE 27. Comparison of the proposed UAS+O based supercapacitor model parameter estimation method with Zubieta's method [5].

FIGURE 28. Validation of the supercapacitor model via the model and parameters found using Zubieta's method [5], as stated in Section VII, with terminal voltage as input, and current as output. Voltage and current data used is the same as in Fig. 18.

in this work. The advantages of the proposed approach are discussed briefly in the next section.

VIII. ADVANTAGES OF THE PROPOSED UAS+O APPROACH

The major advantage of the proposed method is that unlike the method in [5], no 'events' and the voltage and current corresponding to such specific events need to be identified. Further the events mentioned in [5] appear to be based on typical operational observations. So, if a supercapacitor's behavior changes from the typically observed nominal behavior due to aging, there is a greater chance of error in the predicted output using the model in [5]. Further, in event 3 in [5] one has to wait until a measured voltage reaches the rated terminal voltage. This may not be feasible in all scenarios, especially when a supercapacitor is in operation, or if a supercapacitor's

characteristics have altered over-time such that it no longer reaches the rated voltage, but reaches a voltage value near it. Most importantly however, [5] does not provide the input current waveforms used and also does not show the results on different types of inputs. Whereas, the work in this paper is validated on different types of inputs, and is also reverse validated.

Also, the approach proposed in the paper can be allowed to run automatically at preset time intervals, or when it is observed that the predicted output voltage or current do not satisfactorily match the experimentally observed ones. This enables continuous update of supercapacitor model parameters. And helps capture the effects of aging. Further, as shown in [37] the UAS based methods produce accurate parameter estimates with very low computation cost. Also using
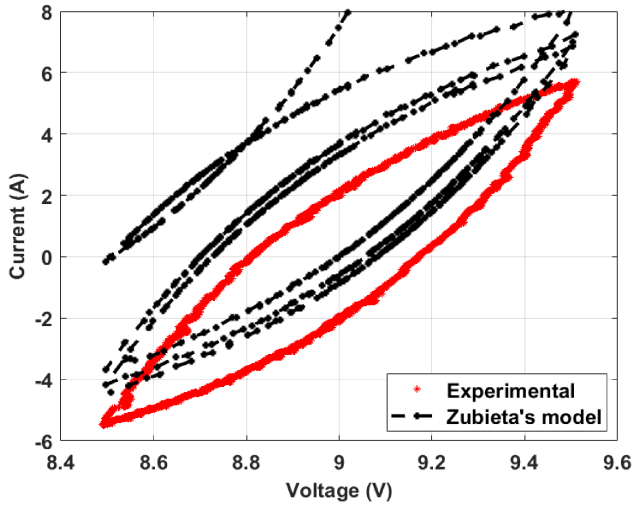
FIGURE 29. V-I curve based on Fig. 28.

optimization methods along with UAS results in increasing estimation accuracy and reducing computation time requirements substantially, compared to other well-known optimization methods [37]. This is because, the UAS based stage provides initial guesses used by the optimization stage to further refine the estimates of model parameter values. This process takes lesser time to converge to parameter values providing good model output, compared to the case of blindly setting bounds on, and providing initial guesses of the parameters being estimated via optimization.

It is worth mentioning that the assumptions required for the mathematical results to hold are not necessarily restrictive, as explained in Section IV.D. Also the requirement for certain vectors to not be in the null-space of other vectors, sort of indirectly hints that the input signal used must be sufficiently rich. This may be circumvented by using inputs satisfying the persistence of excitation (P.E.) condition, which as explained in [38], simply involves the use of signals having a sufficient number of sinusoids. An advantage of using a UAS based approach is that, a Nussbaum function by definition is an oscillatory function whose magnitude and frequency continuously varies, thus making it suited for the task at hand. A complete examination of the P.E. condition, and its use with UAS is beyond the scope of the current work and is left for future efforts.

IX. CONCLUSION
This paper presented a simplified model for a supercapacitor (SC) which can represent SC dynamics sufficiently accurately. An advantage of this model is that it is simpler and thus easier to deal with. Furthermore, offline and online model parameters estimation techniques based on analytic derivation of step, ramp responses, and universal adaptive stabilization were presented respectively. An optimization based approach was used to convert the simplified model into an equivalent RC-ladder network representation. All models and estimated

parameters showed superior performance when estimating the terminal voltage with the current as input. The experimental results presented show, the proposed approaches outperform one of the existing and widely known supercapacitor parameter estimation techniques available in the literature. Future work may involve using the techniques developed in this paper to aid in the estimation of supercapacitor state-of-charge.

APPENDIX
A. PROOF OF LEMMA 4.D.1
Equation (23) can be re-written as follows.

$$\dot{\hat{a}}_n(t) = -\left(\lambda_{xn} + \lambda_{yn}\right)\hat{a}_n(t) + e^2(t) + \lambda_{xn}a_{nu} + \lambda_{yn}a_{nl}$$

Utilizing facts about the solution of a stable linear time invariant (LTI) system, the solution of the above equation gives

$$\hat{a}_n(t) = \hat{a}_n(t_0)\exp\left(-\left(\lambda_{xn} + \lambda_{yn}\right)t\right)$$
$$+ b_1\int_{t_0}^{t}\exp\left(-\left(\lambda_{xn} + \lambda_{yn}\right)\tau\right)d\tau$$
$$+ \int_{t_0}^{t}e^2(t-\tau)\exp\left(-\left(\lambda_{xn} + \lambda_{yn}\right)\tau\right)d\tau \quad (28)$$

where $b_1 = \lambda_{xn}a_{nu} + \lambda_{yn}a_{nl}$. Because the term $\exp(-(\lambda_{xn} + \lambda_{yn})\tau)$ is positive and tends to zero as $t \to \infty$, $a_{nu}, a_{nl}, \lambda_{xn}$, and λ_{yn} are non-negative real numbers, and because $e^2(t-\tau)$, $\hat{a}_n(t_0)$ are also positive, therefore we have proved that $\hat{a}_n(t) > 0$ for all time $t \in [t_0, \infty)$, for all $n \in \{1, \ldots, 4\}$.

B. PROOF OF THEOREM 4.D.2
Let $e(t)$ be as given in (20), and consider the time-derivative, i.e.,

$$\dot{e}(t) = \dot{y}(t) - \dot{\hat{y}}(t) \quad (29)$$

Add and subtract e(t) to the R.H.S., use the definition of $e(t)$ from (20) and re-arrange terms to get the following.

$$\dot{e} = -e - \hat{y} - \dot{\hat{y}} + y + \dot{y} \quad (30)$$

In the above, and in all following equations, the arguments of functions have been skipped for convenience. Using the definition of $\hat{y}$ in (17) with (30) gives

$$\dot{e} = -e - \left(y_{off} + \hat{x}_1 + \hat{x}_2 + \hat{a}_1u\right)$$
$$- \left(\dot{\hat{x}}_1 + \dot{\hat{x}}_2 + \dot{\hat{a}}_1u + \dot{u}\hat{a}_1\right) + y + \dot{y}. \quad (31)$$

Now let $\gamma = -(\dot{\hat{a}}_1u + \dot{u}\hat{a}_1)$, then (31) can be re-written as,

$$\dot{e} = -e - \left(y_{off} + \hat{x}_1 + \dot{\hat{x}}_1\right) - \hat{a}_1u - \left(\hat{x}_2 + \dot{\hat{x}}_2\right) + \gamma + y + \dot{y}. \quad (32)$$

Substituting $\dot{\hat{x}}_1, \dot{\hat{x}}_2$ from (15), (16) into (32) provides

$$\dot{e} = -e - \left(y_{off} + \hat{x}_1 + \frac{u}{\hat{a}_2} + u_a\right) - \hat{a}_1u$$
$$- \left(\hat{x}_2 - \frac{\hat{x}_2}{\hat{a}_4\hat{a}_3} + \frac{u}{\hat{a}_4} + u_a\right) + \gamma + y + \dot{y}. \quad (33)$$

Further let $\delta = -u\left(\frac{1}{\hat{a}_2} + \frac{1}{\hat{a}_4}\right) + \gamma + \dot{y}$, then (33) becomes,

$$\dot{e} = -e - \left(y_{off} + \hat{x}_1 + \hat{x}_2\left(1 - \frac{1}{\hat{a}_4\hat{a}_3}\right) + \hat{a}_1 u\right)$$
$$- 2u_a + y + \delta. \qquad (34)$$

By using Lemma 4.D.1 we know that $\hat{a}_4(t)\hat{a}_3(t) > 0$ for all time $t \in [t_0, \infty)$. Also, from the description following the adaptive observer equations i.e., (15)-(17) we have $\hat{x}_2(t) \geq 0$ for all time $t \in [t_0, \infty)$. Therefore, we have,

$$\hat{x}_2 - \frac{\hat{x}_2}{\hat{a}_4\hat{a}_3} \leq \hat{x}_2. \qquad (35)$$

Adding y_{off}, $\hat{x}_1$, $\hat{a}_1 u$ to both sides of (35) results in:

$$y_{off} + \hat{x}_1 + \hat{x}_2\left(1 - \frac{1}{\hat{a}_4\hat{a}_3}\right) + \hat{a}_1 u \leq y_{off} + \hat{x}_1 + \hat{x}_2 + \hat{a}_1 u \qquad (36)$$

By multiplying both sides of (36) by -1, and then substituting $\hat{y}$ from (17) into the R.H.S. of equation (36) we get,

$$-\left(y_{off} + \hat{x}_1 + \hat{x}_2\left(1 - \frac{1}{\hat{a}_4\hat{a}_3}\right) + \hat{a}_1 u\right) \geq -\hat{y}. \qquad (37)$$

Now add $-e + y - 2u_a + \delta$ to both sides of (37), and then use (34) to obtain,

$$\dot{e} \geq -e + y - \hat{y} - 2u_a + \delta. \qquad (38)$$

Using the definition of e from (20) gives,

$$\dot{e} \geq -2u_a + \delta. \qquad (39)$$

Let,

$$V(e, u_a) = \frac{1}{2}e^2 - 2\int_{k(t_0)}^{k(t)} N(\tau)\,d\tau, \qquad (40)$$

then,

$$\dot{V} = e\dot{e} - 2N(k(t))e^2(t). \qquad (41)$$

Now consider the following cases with respect to $e(t)$,
Case 1: $e(t) < 0$
Using (39), and then (18) with (41) gives,

$$\dot{V} \leq e\delta. \qquad (42)$$

Because $(e - \delta)^2 \geq 0$ for all time, therefore we have $\frac{1}{2}(e^2 + \delta^2) \geq e\delta$. Now (42) can be re-written as follows.

$$\dot{V}(e, u_a) \leq \frac{1}{2}(e^2 + \delta^2) \qquad (43)$$

Integrate the above to get,

$$V(e(t), u_a(t)) - V(e(t_0), u_a(t_0)) \leq \frac{1}{2}\int_{t_0}^{t} e^2(\tau)\,d\tau$$
$$+ \frac{1}{2}\int_{t_0}^{t} \delta^2(\tau)\,d\tau. \qquad (44)$$

From (19) we know that $\frac{1}{2}\int_{t_0}^{t} e^2(\tau)d\tau = \frac{1}{2}(k(t) - k(t_0))$. Let $(k(t) - k(t_0)) = \tilde{k}(t)$, substitute $V(\cdot, \cdot)$ from (40) into (44)

and re-arrange to get the following.

$$\frac{e^2(t)}{2\tilde{k}(t)} \leq \frac{1}{2} + \frac{V(e(t_0), u_a(t_0))}{\tilde{k}(t)}$$
$$+ \frac{1}{2\tilde{k}(t)}\int_{t_0}^{t} \delta^2(\tau)\,d\tau + \frac{2}{\tilde{k}(t)}\int_{k(t_0)}^{k(t)} N(\tau)\,d\tau \qquad (45)$$

Notice that by the definition in (19), $\tilde{k}(t) = (k(t) - k(t_0)) > 0$. Also, recall that the term $\delta(t) = -u(t)\left(\frac{1}{\hat{a}_2(t)} + \frac{1}{\hat{a}_4(t)}\right) - \dot{\hat{a}}_1(t)u(t) - \dot{u}(t)\hat{a}_1(t) + \dot{y}(t)$.
Suppose $k(t) \to \infty$ as $t \to \infty$. From the assumptions we know that as $t \to \infty$, then $u(t)$, $\dot{u}(t)$, and $\dot{y}(t)$ tends to zero. Also from Lemma 4.D.1 we know that $\hat{a}_2(t)$, and $\hat{a}_4(t)$ are positive for all time. So as $t \to \infty$ we have $\delta(t) \to 0$. Because the numerators of the second and third terms on the R.H.S. of (45) are bounded, taking the limit as $k(t) \to \infty$ gives,

$$\frac{e^2(t)}{2\tilde{k}(t)} \leq \frac{1}{2} + \frac{2}{\tilde{k}(t)}\int_{k(t_0)}^{k(t)} N(\tau)\,d\tau \qquad (46)$$

The L.H.S. in (46) is always non-negative, however if $k(t) \to \infty$ as $t \to \infty$, then by the definition of a Nussbaum function in Section IV.B., the R.H.S. in (46) is free to take arbitrary negative values. This violates the non-negativity of the L.H.S. in (46). By this contradiction, it is possible to say that $k(t)$ cannot go to infinity with time, i.e., it is bounded. However by definition in (19) we know that $\dot{k}(t) > 0$, i.e., as $t \to \infty$, $k(t)$ must tend to some constant k_∞. And therefore by (19) we have $\dot{k}(t) \to 0$, i.e., $e(t) \to 0$. Now consider the below case.
Case 2: $e(t) > 0$
Using (39), and then (18) with (41) gives, in this case,

$$\dot{V} \geq e\delta. \qquad (47)$$

As discussed between (42), (43) we have $\frac{1}{2}(e^2 + \delta^2) \geq e\delta$. This, along with (47) gives rise to two further possibilities:
Case 2.1:

$$\dot{V}(e, u_a) \geq \frac{1}{2}(e^2 + \delta^2) \geq e\delta \qquad (48)$$

or,
Case 2.2:

$$\frac{1}{2}(e^2 + \delta^2) \geq \dot{V}(e, u_a) \geq e\delta \qquad (49)$$

Notice that the upper bound on $\dot{V}$ in (49) leads to $\dot{V}(e, u_a) \leq \frac{1}{2}(e^2 + \delta^2)$, i.e., the same condition as in (43). So the proof for Case 2.2 proceeds, from this point on, exactly as Case 1. Now consider Case 2.1, i.e., $\dot{V}(e, u_a) \geq \frac{1}{2}(e^2 + \delta^2)$ and integrate to get

$$V(e(t), u_a(t)) - V(e(t_0), u_a(t_0)) \geq \frac{1}{2}\int_{t_0}^{t} e^2(\tau)\,d\tau$$
$$+ \frac{1}{2}\int_{t_0}^{t} \delta^2(\tau)\,d\tau. \qquad (50)$$

From (19) it is known that $\frac{1}{2}\int_{t_0}^t e^2(\tau)d\tau = \frac{1}{2}(k(t) - k(t_0))$. Further, letting $(k(t) - k(t_0)) = \tilde{k}(t)$, substituting $V(\cdot, \cdot)$ from (40) into (50) and re-arranging gives the following.

$$\frac{e^2(t)}{2\tilde{k}(t)} \geq \frac{1}{2} + \frac{V(e(t_0), u_a(t_0))}{\tilde{k}(t)}$$
$$+ \frac{1}{2\tilde{k}(t)}\int_{t_0}^t \delta^2(\tau)d\tau + \frac{2}{\tilde{k}(t)}\int_{k(t_0)}^{k(t)} N(\tau)d\tau \tag{51}$$

Consider the following cases with regard to (51),
Case 2.2.1

$$\frac{e^2(t)}{2\tilde{k}(t)} \geq \left(\frac{1}{2} + \frac{V(e(t_0), u_a(t_0))}{\tilde{k}(t)}\right.$$
$$\left.+ \frac{1}{2\tilde{k}(t)}\int_{t_0}^t \delta^2(\tau)d\tau + \frac{2}{\tilde{k}(t)}\int_{k(t_0)}^{k(t)} N(\tau)d\tau\right) > 0 \tag{52}$$

Case 2.2.2

$$\frac{e^2(t)}{2\tilde{k}(t)} \geq 0 \geq \left(\frac{1}{2} + \frac{V(e(t_0), u_a(t_0))}{\tilde{k}(t)}\right.$$
$$\left.+ \frac{1}{2\tilde{k}(t)}\int_{t_0}^t \delta^2(\tau)d\tau + \frac{2}{\tilde{k}(t)}\int_{k(t_0)}^{k(t)} N(\tau)d\tau\right) \tag{53}$$

Let's start with Case 2.2.2, suppose at some time instant t^*, (53) is satisfied, and suppose now that as $t \to \infty, t \geq t^*$ then $k(t) \to \infty$. Then by the definition of a Nussbaum function, $\frac{2}{\tilde{k}(t)}\int_{k(t_0)}^{k(t)} N(\tau)d\tau$ could take values $\to \infty$. As shown in Case 1, the remaining terms $\frac{1}{2}$, $\frac{V(e(t_0), u_a(t_0))}{\tilde{k}(t)}$, $\frac{1}{2\tilde{k}(t)}\int_{t_0}^t \delta^2(\tau)d\tau$, are constant, tending to zero, and bounded respectively. So as $\frac{2}{\tilde{k}(t)}\int_{k(t_0)}^{k(t)} N(\tau)d\tau$ increases towards infinity, consider an intermediate instant of time $t' > t^*$ where $\frac{2}{\tilde{k}(t)}\int_{k(t_0)}^{k(t)} N(\tau)d\tau$ is positive and large enough giving,

$$\frac{e^2(t)}{2\tilde{k}(t)} \geq \left(\frac{1}{2} + \frac{V(e(t_0), u_a(t_0))}{\tilde{k}(t)}\right.$$
$$\left.+ \frac{1}{2\tilde{k}(t)}\int_{t_0}^t \delta^2(\tau)d\tau + \frac{2}{\tilde{k}(t)}\int_{k(t_0)}^{k(t)} N(\tau)d\tau\right) > 0.$$

Notice that the above is the same as Case 2.2.1, i.e., showing if Case 2.2.2 does occur, then this eventually leads to Case 2.2.1 occurring. Because all quantities in (52) for Case 2.2.1 have the same sign so it is possible to write the following

$$\frac{2\tilde{k}(t)}{e^2(t)} \leq h(t) \tag{54}$$

$$h(t) = \left(\frac{1}{2} + \frac{V(e(t_0), u_a(t_0))}{\tilde{k}(t)}\right.$$
$$\left.+ \frac{1}{2\tilde{k}(t)}\int_{t_0}^t \delta^2(\tau)d\tau + \frac{2}{\tilde{k}(t)}\int_{k(t_0)}^{k(t)} N(\tau)d\tau\right)^{-1} \tag{55}$$

Now suppose $k(t) \to \infty$ as $t \to \infty$. The L.H.S. in (54) is always positive, however if $k(t) \to \infty$ as $t \to \infty$, then as shown earlier, all other terms other than the Nussbaum function are bounded. And by the definition of a Nussbaum function in Section IV.B., $h(t)$ in (54), (55) can take negative values, this contradicts the positiveness of the L.H.S. in (54), and thus as shown at the end of Case 1, gives us the required result i.e., as $t \to \infty$, $k(t)$ must tend to some constant k_∞. And therefore by (19) we have $\dot{k}(t) \to 0$, i.e., $e(t) \to 0$.

C. PROOF OF THEOREM 4.D.3
Because the assumptions required for Theorem 4.D.2 to hold are satisfied, so by Theorem 4.D.2 we can write $e(t) \to 0$ as $t \to \infty$, i.e., $y(t) - \hat{y}(t) \to 0$ as $t \to \infty$. Further, using the definition of $y(t)$ in (14), and the definition of $\hat{y}(t)$ in (17), it is possible to write the following.

$$\begin{bmatrix} 1 & 1 & u(t) \end{bmatrix} \begin{bmatrix} x_1(t) - \hat{x}_1(t) \\ x_2(t) - \hat{x}_2(t) \\ R_p - \hat{a}_1(t) \end{bmatrix} \to 0, \tag{56}$$

Notice that (56) is the same as writing $\bar{v}_1(t)\bar{v}_2(t) \to 0$. Suppose $t > T$, and $t \to \infty$. Because $u(t) \neq 0$, and by the assumptions of this theorem, we have $\bar{v}_2(t)$ is not in the null space of $\bar{v}_1(t)$. Thus, the only way the L.H.S. in (56) can tend to zero is if $\hat{x}_1(t) \to x_1(t)$, $\hat{x}_2(t) \to x_2(t)$, and $\hat{a}_1(t) \to R_p$. So consider $\hat{x}_1(t) \to x_1(t)$ and take time derivatives of both sides. This gives,

$$\frac{u(t)}{\hat{a}_2(t)} + u_a(t) \to \frac{u(t)}{C_p}, \tag{57}$$

And $u_a(t) \to 0$ as $t \to \infty$, because $u_a(t) = -N(k(t))e(t)$, and from Theorem 4.D.2. we have that $e(t) \to 0$ as $t \to \infty$. Using these facts with (57) leads to $\hat{a}_2(t) \to C_p$ as $t \to \infty$. Similarly considering $\hat{x}_2(t) \to x_2(t)$, taking time derivatives of both sides, and using the fact that $u_a(t) \to 0$ as $t \to \infty$, we can write the following.

$$-\frac{\hat{x}_2(t)}{\hat{a}_4(t)\hat{a}_3(t)} + \frac{u(t)}{\hat{a}_4(t)} = -\frac{x_2(t)}{C_0 R_0} + \frac{u(t)}{C_0} \tag{58}$$

Further utilizing the fact that $\hat{x}_2(t) \to x_2(t)$, and re-arranging (58) provides,

$$\begin{bmatrix} x_2(t) & u(t) \end{bmatrix} \begin{bmatrix} \left(\frac{1}{C_0 R_0} - \frac{1}{\hat{a}_4(t)\hat{a}_3(t)}\right) \\ \left(\frac{1}{\hat{a}_4(t)} - \frac{1}{C_0}\right) \end{bmatrix} \to 0. \tag{59}$$

Notice that (59) is the same as writing $\bar{v}_3(t)\bar{v}_4(t) \to 0$. Because $x_2(t) \neq 0$, $u(t) \neq 0$, and by the assumptions of this theorem we have $\bar{v}_4(t)$ is not in the null space of $\bar{v}_3(t)$. So from (59) it is possible to get $\hat{a}_4(t) \to C_0$, which further gives $\hat{a}_3(t) \to R_0$ as $t \to \infty$. This proves the required result, i.e., $\hat{a}_1(t) \to R_p$, $\hat{a}_2(t) \to C_p$, $\hat{a}_3(t) \to R_0$, $\hat{a}_4(t) \to C_0$ as $t \to \infty$.

REFERENCES

[1] M. Ammar and G. Joos, "A short-term energy storage system for voltage quality improvement in distributed wind power," *IEEE Trans. Energy Convers.*, vol. 29, no. 4, pp. 997–1007, Dec. 2014.

[2] M. Mellincovsky *et al.*, "Performance and limitations of a constant power-fed supercapacitor," *IEEE Trans. Energy Convers.*, vol. 29, no. 2, pp. 445–452, Jun. 2014.

[3] P. Thounthong, "Model based-energy control of a solar power plant with a supercapacitor for grid-independent applications," *IEEE Trans. Energy Convers.*, vol. 26, no. 4, pp. 1210–1218, Dec. 2011.

[4] F. A. Inthamoussou, J. Pegueroles-Queralt, and F. D. Bianchi, "Control of a supercapacitor energy storage system for microgrid applications," *IEEE Trans. Energy Convers.*, vol. 28, no. 3, pp. 690–697, Sep. 2013.

[5] L. Zubieta and R. Bonert, "Characterization of double-layer capacitors for power electronics applications," *IEEE Trans. Ind. Appl.*, vol. 36, no. 1, pp. 199–205, 2000.

[6] D. Torregrossa, M. Bahramipanah, E. Namor, R. Cherkaoui, and M. Paolone, "Improvement of dynamic modeling of supercapacitor by residual charge effect estimation," *IEEE Trans. Ind. Electron.*, vol. 61, no. 3, pp. 1345–1354, Mar. 2014.

[7] S. Fletcher, V. J. Black, and I. Kirkpatrick, "A universal equivalent circuit for carbon-based supercapacitors," *J. Solid State Electrochem.*, vol. 18, no. 5, pp. 1377–1387, 2014.

[8] A. Nadeau, G. Sharma, and T. Soyata, "State-of-charge estimation for supercapacitors: A Kalman filtering formulation," in *Proc. IEEE Int. Conf. Acoustics, Speech Signal Process.*, 2014, pp. 2194–2198.

[9] N. Reichbach and A. Kuperman, "Recursive-least-squares-based real-time estimation of supercapacitor parameters," *IEEE Trans. Energy Convers.*, vol. 31, no. 2, pp. 810–812, Jun. 2016.

[10] S. Buller, M. Thele, R. W. DeDoncker, and E. Karden, "Impedance-based simulation models of supercapacitors and Li-Ion batteries for power electronic applications," *IEEE Trans. Ind. Appl.*, vol. 41, no. 3, pp. 742–747, May 2005.

[11] N. Bertrand, J. Sabatier, O. Briat, and J. M. Vinassa, "Embedded fractional nonlinear supercapacitor model and its parametric estimation method," *IEEE Trans. Ind. Electron.*, vol. 57, no. 12, pp. 3991–4000, Dec. 2010.

[12] N. Bertrand, J. Sabatier, J.-M. Vinassa, and O. Briat, "A new nonlinear supercapacitor embedded model and its online time identification method," in *Proc. ASME Int. Des. Eng. Tech. Conf. Comput. Inf. Eng. Conf.*, 2009, pp. 1233–1240.

[13] T. Funaki and T. Hikihara, "Characterization and modeling of the voltage dependency of capacitance and impedance frequency characteristics of packed EDLCs," *IEEE Trans. Power Electron.*, vol. 23, no. 3, pp. 1518–1525, May 2008.

[14] S. Barcellona, F. Ciccarelli, D. Iannuzzi, and L. Piegari, "Overview of lithium-ion capacitor applications based on experimental performances," *Electric Power Compon. Syst.*, vol. 44, no. 11, pp. 1248–1260, May 2016.

[15] S. Barcellona, F. Ciccarelli, D. Iannuzzi, and L. Piegari, "Modeling and parameter identification of lithium-ion capacitor modules," *IEEE Trans. Sustainable Energy*, vol. 5, no. 3, pp. 785–794, Jul. 2014.

[16] A. Krause, P. Kossyrev, M. Oljaca, S. Passerini, M. Winter, and A. Balducci, "Electrochemical double layer capacitor and lithium-ion capacitor based on carbon black," *J. Power Sources*, vol. 196, no. 20, pp. 8836–8842, Oct. 2011.

[17] Z. Stevic, M. Rajcic-Vujasinovic, and I. Radovanovic, "Comparative analysis of dynamic electrochemical test methods of supercapacitors," *Int. J. Electrochemical Sci.*, vol. 9, no. 12, pp. 7110–7130, 2014.

[18] N. Rizoug, P. Bartholomeus, and P. Le Moigne, "Study of the ageing process of a supercapacitor module using direct method of characterization," *IEEE Trans. Energy Convers.*, vol. 27, no. 2, pp. 220–228, Jun. 2012.

[19] Y. Cheng, "Assessments of energy capacity and energy losses of supercapacitors in fast charging–discharging cycles," *IEEE Trans. Energy Convers.*, vol. 25, no. 1, pp. 253–261, Mar. 2010.

[20] L. Liu, L. Y. Wang, Z. Chen, C. Wang, F. Lin, and H. Wang, "Integrated system identification and state-of-charge estimation of battery systems," *IEEE Trans. Energy Convers.*, vol. 28, no. 1, pp. 12–23, Mar. 2013.

[21] F. Belhachemi, S. Rael, and B. Davat, "A physical based model of power electric double-layer supercapacitors," in *Proc. Conf. Rec. 2000 IEEE Ind. Appl. Conf.*, 2000, pp. 3069–3076.

[22] D. Ali, S. Mukhopadhyay, and H. Rehman, "A novel adaptive technique for Li-ion battery model parameters estimation," in *Proc. IEEE Nat. Aerosp. Electron. Conf., NAECON*, 2017, pp. 23–26.

[23] D. Ali, S. Mukhopadhyay, H. Rehman, and A. Khurram, "UAS based Li-ion battery model parameters estimation," *Control Eng. Pract.*, vol. 66, pp. 126–145, 2017. [Online]. Available: https://www.sciencedirect.com/science/article/pii/S0967066117301387

[24] S. Mukhopadhyay and F. Zhang, "A high-gain adaptive observer for detecting Li-ion battery terminal voltage collapse," *Automatica*, vol. 50, no. 3, pp. 896–902, Mar. 2014.

[25] I. Podlubny, I. Petráš, B. M. Vinagre, P. O'Leary, and L. Dorčák, "Analogue realizations of fractional-order controllers," *Nonlinear Dyn.*, vol. 29, pp. 281–296, 2002.

[26] H. Sheng, Y. Chen, and T. Qiu, in *Fractional Processes and Fractional-Order Signal Processing*. Berlin, Germany: Springer, 2012.

[27] C. D. Olds, in *Continued Fractions*. WA, DC, USA: The Mathematical Association of America, 1963.

[28] V. Musolino, L. Piegari, and E. Tironi, "New full-frequency-range supercapacitor model with easy identification procedure," *IEEE Trans. Ind. Electron.*, vol. 60, no. 1, pp. 112–120, Jan. 2013.

[29] D. W. Marquardt, "An algorithm for least-squares estimation of nonlinear parameters," *J. Soc. Ind. Appl. Math.*, vol. 11, no. 2, pp. 431–441, Jun. 1963.

[30] N. Yamashita and M. Fukushima, "On the rate of the convergence of the Levenberg-Marquardt method," *Comput.*, vol. 15, pp. 239–249, 2001.

[31] H. Gavin, "The Levenberg-Marquardt method for nonlinear least squares curve-fitting problems," Department of Civil and Environmental Engineering, Duke University. [Online]. Available: http://people.duke.edu/~hpgavin/ce281/lm.pdf

[32] X.-L. Luo, L.-Z. Liao, and H. Wah Tam, "Convergence analysis of the Levenberg–Marquardt method," *Optim. Methods Softw.*, vol. 22, no. 4, pp. 659–678, Aug. 2007.

[33] A. Ilchmann, in *Non-Identifier-Based High-Gain Adaptive Control, Lecture Notes in Control and Information Sciences, 189*. Berlin, Germany: Springer-Verlag, 1993.

[34] Y. Li and Y. Chen, "When is a Mittag-Leffler function a Nussbaum function?" *Automatica*, vol. 45, no. 8, pp. 1957–1959, 2009.

[35] S. Mukhopadhyay, Y. Li, and Y. Chen, "Experimental studies of a fractional order universal adaptive stabilizer," in *Proc. IEEE/ASME Int. Conf. Mechatronic Embedded Syst. Appl.*, 2008, pp. 591–596.

[36] Open Source Motor Control (OSMC) Product Information, [Online]. Available: http://www.robotpower.com/products/osmc_info.html

[37] H. M. Usman, S. Mukhopadhyay, and H. Rehman, "Universal adaptive stabilizer based optimization for Li-ion battery model parameters estimation: An experimental study," *IEEE Access*, vol. 6, pp. 49546–49562, 2018.

[38] H. M. Usman, S. Mukhopadhyay, and H. Rehman, "Permanent magnet DC motor parameters estimation via universal adaptive stabilization," *Control Eng. Pract.*, vol. 90, pp. 50–62, 2019.